IMAGE PROCESSING METHODS FOR COMPUTER-AIDED INTERPRETATION OF MICROSCOPIC IMAGES

A THESIS

SUBMITTED TO THE DEPARTMENT OF ELECTRICAL AND

ELECTRONICS ENGINEERING

AND THE GRADUATE SCHOOL OF ENGINEERING AND SCIENCE

OF BILKENT UNIVERSITY

IN PARTIAL FULFILLMENT OF THE REQUIREMENTS

FOR THE DEGREE OF

MASTER OF SCIENCE

By

Musa Furkan Keskin

September, 2012

I certify that I have read this thesis and that in my opinion it is fully adequate, in scope and in quality, as a thesis for the degree of Master of Science.

Prof. Dr. A. Enis Çetin(Advisor)

I certify that I have read this thesis and that in my opinion it is fully adequate, in scope and in quality, as a thesis for the degree of Master of Science.

Asst. Prof. Dr. Sinan Gezici

I certify that I have read this thesis and that in my opinion it is fully adequate, in scope and in quality, as a thesis for the degree of Master of Science.

Assoc. Prof. Dr. Uğur Güdükbay

Approved for the Graduate School of Engineering and Science:

Prof. Dr. Levent Onural
Director of the Graduate School

ABSTRACT

IMAGE PROCESSING METHODS FOR COMPUTER-AIDED INTERPRETATION OF MICROSCOPIC IMAGES

Musa Furkan Keskin
M.S. in Electrical and Electronics Engineering
Supervisor: Prof. Dr. A. Enis Çetin
September, 2012

Image processing algorithms for automated analysis of microscopic images have become increasingly popular in the last decade with the remarkable growth in computational power. The advent of high-throughput scanning devices allows for computer-assisted evaluation of microscopic images, resulting in a quick and unbiased image interpretation that will facilitate the clinical decision-making process. In this thesis, new methods are proposed to provide solution to two image analysis problems in biology and histopathology.

The first problem is the classification of human carcinoma cell line images. Cancer cell lines are widely used for research purposes in laboratories all over the world. In molecular biology studies, researchers deal with a large number of specimens whose identity have to be checked at various points in time. A novel computerized method is presented for cancer cell line image classification. Microscopic images containing irregular carcinoma cell patterns are represented by subwindows which correspond to foreground pixels. For each subwindow, a covariance descriptor utilizing the dual-tree complex wavelet transform (DT-CWT) coefficients as pixel features is computed. A Support Vector Machine (SVM) classifier with radial basis function (RBF) kernel is employed for final classification. For 14 different classes, we achieve an overall accuracy of 98%, which outperforms the classical covariance based methods.

Histopathological image analysis problem is related to the grading of follicular lymphoma (FL) disease. FL is one of the commonly encountered cancer types in the lymph system. FL grading is based on histological examination of hematoxilin and eosin (H&E) stained tissue sections by pathologists who make clinical decisions by manually counting the malignant centroblast (CB) cells. This grading

method is subject to substantial inter- and intra-reader variability and sampling bias. A computer-assisted method is presented for detection of CB cells in H&E-stained FL tissue samples. The proposed algorithm takes advantage of the scale-space representation of FL images to detect blob-like cell regions which reside in the scale-space extrema of the difference-of-Gaussian images. Multi-stage false positive elimination strategy is employed with some statistical region properties and textural features such as gray-level co-occurrence matrix (GLCM), gray-level run-length matrix (GLRLM) and Scale Invariant Feature Transform (SIFT). The algorithm is evaluated on 30 images and 90% CB detection accuracy is obtained, which outperforms the average accuracy of expert hematopathologists.

Keywords: Cancer Cell Line Classification, Dual-Tree Complex Wavelet Transform, Covariance Descriptors, Follicular Lymphoma Grading, Scale-Space Representation, Centroblast Detection, Blob Detection, Scale Invariant Feature Transform.

ÖZET

MİKROSKOPİK GÖRÜNTÜLERİN BİLGİSAYAR DESTEKLİ YORUMLANMASI İÇİN İMGE İŞLEME YÖNTEMLERİ

Musa Furkan Keskin
Elektrik ve Elektronik Mühendisliği Bölümü, Yüksek Lisans
Tez Yöneticisi: Prof. Dr. A. Enis Çetin
Eylül, 2012

Hesaplama gücündeki kayda değer büyüme ile birlikte, imge işleme algoritmalarının mikroskopik görüntülerin otomatik analizinde kullanımı son on yılda giderek popüler hale gelmiştir. Yüksek işlem hacimli tarama cihazlarının ortaya çıkışı mikroskopik görüntülerin bilgisayar destekli yorumlanmasına imkan tanımıştır. Bu gelişme, klinik karar alma süreçlerini kolaylaştıracak olan hızlı ve objektif görüntü yorumlama sonucunu doğurmuştur. Bu tezde, biyoloji ve histopatoloji alanlarından iki görüntü analizi problemine çözüm üretme amacıyla, yeni yöntemler sunulmuştur.

Bu problemlerden ilki, insandan elde edilen kanser hücre çizgi görüntülerinin sınıflandırılmasıdır. Kanser hücre çizgileri tüm dünyada laboratuvarlarda araştırma amacıyla yaygın bir biçimde kullanılmaktadır. Moleküler biyoloji çalışmalarında araştırmacılar, ait olduğu sınıf sürekli olarak doğrulanması gereken çok sayıda numune ile çalışmaktadır. Kanser hücre çizgi görüntülerinin sınıflandırılması için özgün bir bilgisayar destekli yöntem sunulmuştur. Düzensiz kanser hücre paternleri içeren mikroskop görüntüleri, önplan piksellerine karşılık gelen yerel pencereler ile temsil edilmiştir. Her yerel pencere için, çift-ağaç karmaşık dalgacık dönüşümü (DT-CWT) katsayılarını piksel öznitelikleri olarak kullanan bir kovaryans tanımlayıcısı hesaplanmıştır. Sınıflandırma amacıyla RBF çekirdekli Destek Vektör Makinası (SVM) kullanılmıştır. 14 farklı sınıf için, % 98 ortalama doğruluk oranı elde edilmiştir, ki bu klasik kovaryans tabanlı yöntemlerden daha iyi bir sonuçtur.

Histopatolojik görüntü analizi problemi ise foliküler lenfoma (FL) hastalığının derecelendirilmesi ile ilgilidir. FL, lenf sisteminde sık karşılaşılan kanser

çeşitlerinden biridir. FL derecelendirmesi, hematoksilin ve eozin (H&E) ile lekelendirilmiş doku parçalarının patologlar tarafından histolojik incelemeye tabi tutulması ile gerçekleştirilir ve patologlar kötü huylu sentroblast (CB) hücrelerini el ile sayarak klinik kararlar alırlar. Bu derecelendirme yöntemi, gözlemci içinde ve gözlemciler arasında ciddi bir değişkenlik ve örnekleme kaynaklı hatalar ile karşı karşıyadır. H&E lekeli FL doku örneklerinde CB hücrelerinin tespiti amacıyla bilgisayar destekli bir yöntem sunulmuştur. Önerilen algoritma, Gauss farkı görüntülerinin ölçek-alan uçdeğerlerinde yer alan blob benzeri hücre bölgelerini tespit etmek için, FL görüntülerinin ölçek-alan temsilinden faydalanmaktadır. Bazı istatistiksel bölge öznitelikleri ve gri-düzey birliktelik matrisi (GLCM), gri-düzey sıra-uzunluk matrisi (GLRLM) ve Ölçek Değişimsiz Öznitelik Dönüşümü (SIFT) gibi dokusal öznitelikler kullanılarak, çok aşamalı yanlış alarm eleme stratejisi uygulanmıştır. Algoritma, 30 görüntü üzerinde değerlendirilmiş ve %90 CB tespit doğruluk oranı elde edilmiştir. Bu oran, uzman hematopatologların ortalama doğruluk oranından üstündür.

Anahtar sözcükler: Kanser Hücre Çizgisi Sınıflandırılması, Çift-Ağaç Karmaşık Dalgacık Dönüşümü, Kovaryans Tanımlayıcıları, Foliküler Lenfoma Derecelendirilmesi, Ölçek-Alan Temsili, Sentroblast Tespiti, Blob Tespiti, Ölçek Değişimsiz Öznitelik Dönüşümü.

Acknowledgement

I would like to express my gratitude to Prof. Dr. Enis Çetin for his supervision, guidance and suggestions throughout the development of this thesis.

I would also like to thank Asst. Prof. Dr. Sinan Gezici and Assoc. Prof. Dr. Uğur Güdükbay for reading, commenting and making suggestions on this thesis.

I wish to extend my thanks to all friends and colleagues for their valuable help in the development of this thesis.

I would also like to thank TÜBİTAK for providing financial support throughout my graduate study.

I would like to thank my colleagues in Clinical Image Analysis Laboratory at The Ohio State University for their support during my Columbus days. Special thanks to Assoc. Prof. Dr. Metin Nafi Gürcan and Dr. Khalid Niazi.

I would like to express my special thanks to my family and my fiancee for their sincere love, support and encouragement.

Contents

List of Figures

List of Tables

Chapter 1

Introduction

Computer-aided clinical image analysis has attracted huge interest from both signal processing and medical researchers due to its potential to surmount the challenges associated with the subjective examination of microscopic images. Quantitative tools for characterization of biomedical images mitigate the effects of inter- and intra-reader variability on diagnosis and complement the clinical decision by acting as a second reader. Computer-assisted diagnosis (CAD) systems can prevent pathologists from wasting their time on image regions where decisions can be made in a straightforward manner; the percentage of the benign prostate biopsies in the U.S. is around 80%, which may be handled by computerized image analysis, leaving more space for pathologists to deal with challenging cases [1]. Biologists would also need automated tools to discriminate between a large number of different cell types since the biochemical tests performed for identification of cells may be very costly. The goal of this thesis is to develop new algorithms for computer-aided analysis of biomedical images by employing image processing and machine learning techniques. The main objective is to devise automated methods for feature detection, extraction and classification that would provide robust interpretation of biological and histopathological images.

In this thesis, two different microsopic image analysis problems are considered. The first part of the thesis focuses on the discrimination of human carcinoma cell line images which are widely used in molecular biology studies. The identity of

cancer cell lines that are employed in cancer research needs to be verified recurringly during a research project. Distinct morphologies of different types and even sub-types of cancer cells reflect, at least in part, the underlying biochemical differences, i.e., gene expression profiles [2]. The morphology of cancer cells can infer invasiveness of tumor cell and hence the metastatic capability. Human cancer cell lines are also utilized in drug screening and development [3]. Hence, mislabeling cell lines or failure to recognize any contamination may lead to misleading results. It is of vital importance to incorporate an automated morphological analysis tool for cancer cells during molecular biology research, that will enable the correct detection and labelling of different cell lines. The change in morphologies upon treatment with agents that induce cellular responses such as cell death or cell growth arrest can also be distinguished with such algorithms [4]. Currently, short tandem repeat (STR) analysis is being used as a standard for the authentication of human cell lines. However, this process takes a long time and has to be carried out by an expert. Automated analysis, on the other hand, will provide the scientists a fast and easy-to-use tool that they can use in their own laboratories to verify their cell lines.

In this thesis, dual-tree complex wavelet transform (DT-CWT) based feature extraction and classification method is developed to differentiate distinct types of cancer cell line images. DT-CWT is a recently developed image decomposition method that possesses orientation selectivity and shift invariance properties lacking in the classical discrete wavelet transform. It has been used in a variety of signal and image processing tasks including denoising [5], classification [6], texture analysis [7], compression [8] and watermarking [9]. In DT-CWT, two maximally decimated discrete wavelet transforms are executed in parallel, where the wavelet functions of two different trees form an approximate Hilbert transform pair, thereby leading to a directionally selective and shift invariant transform [10]. Region covariance descriptors are utilized to construct feature matrices from DT-CWT complex coefficient magnitudes in detail subbands at several decomposition scales. In the region covariance framework each pixel is mapped to a set of pixel properties whose covariances are measured and used

as a region descriptor [11]. It is experimentally observed that the proposed DT-CWT based algorithm generates distinctive features and is superior to classical covariance based methods.

The second microscopic image analysis problem that is addressed in the thesis concerns histopathology imagery. Follicular lymphoma (FL) grading using computer-assisted image analysis is investigated. FL is a cancer type arising in the lymphatic system and it is one of the most commonly encountered lymphoid malignancies in the western world [12]. As recommended by World Health Organization, grading of FL relies on histological examination of hematoxilin and eosin (H&E)-stained tissue sections by pathologists who manually count the average number of large cancerous cells called centroblasts (CB) in ten standard microscopic high-power fields (HPF) and assign each FL case to one of the three grades based on the average CB count per HPF [13]. Qualitative evaluation of FL images by human readers poses serious problems such as inter- and intra-observer variability and sampling bias [14]. Since the choice of ten HPFs for counting CBs is random, heteregenous distribution of malignant cells would make the grading method biased. Moreover, manual counting is a time-consuming and laborious task for pathologists. Computer-aided FL prognosis system is highly required in a clinical setting to guide the pathologist and help reach more accurate clinical decisions. In the literature, model-based intermediate representations (MBIR) are employed to model the distribution of cytological components in FL images and perform grading on an image level [15]. Adaptive likelihood [16] and local fourier transform (LFT) [17] based cell segmentation approaches are also utilized for FL grading.

A new algorithm is proposed in this thesis for computer-aided detection of CB cells in FL images using scale-space representations, which can be defined as the collection of images obtained by successive convolutions with a scale-space kernel. The intuition behind this approach is that CB and non-CB (centrocyte) cells appear as dark blob-like regions in each channel of the H&E stained RGB images of FL. Utilizing the fact that scale-space extrema of the difference-of-Gaussian images correspond to blob-like structures in the image [18], a modified version of the Scale-Invariant Feature Transform (SIFT) algorithm [19] is used

to identify salient regions, which, in this case, are CB and non-CB cells. Identification of candidate CB regions is followed by false positive reduction stages. Most of the false positives can be eliminated based on size information inherently provided by the scale-space processing. At later stages, statistical region features, co-occurrence and run-length properties and SIFT descriptor encoding the texture distribution are employed to further reduce the number of non-CB cells. A comparative analysis of different feature sets points to the fact that SIFT is effective in feature detection, but is outperformed by other texture descriptors in the phase of feature extraction from cell regions. Sensitivity of the whole system is found to be better than the average sensitivity of six expert board-certified pathologists.

The rest of the thesis is organized as follows. Chapter 2 presents the DT-CWT and covariance based image classification framework developed for differentiation of human cancer cell lines. In Chapter 3, a computer-assisted method utilizing the scale-space image representation is proposed to detect centroblast cells for follicular lymphoma grading. In the last chapter, conclusions are made and the contributions are highlighted.

Chapter 2

Human Cancer Cell Line Classification in Microscopic Images

Cancer cell lines are cancer cells derived from human body, which are cultivated in a laboratory environment. They may proliferate in time and spread over dishes where they were first seeded. Human cancer cell lines constitute essential research instruments in scientific molecular biology studies [20, 21]. They are widely utilized in cancer research and drug discovery. However, use of cell lines suffers greatly from cross-contamination with other cell lines [22], misidentification and over-subculturing [21], which may lead to misleading, irrelevant research results and wasting of millions of dollars invested in cancer research [23]. The frequency of inter- and intra-species cross-contamination can be as high as 18-35% and cell misidentification rate can reach up to 18% [24, 25], which are deemed intolerable in the area of cancer and drug research where consequences on human life can be tremendous. Therefore, the identity of cancer cell lines have to be confirmed continuously throughout the course of the research being conducted. Short tandem repeat (STR) profiling was proposed as a method for cell line authentication to preclude data misinterpretation, thereby eliminating the aforementioned

Figure 2.1: Sample cancer cell line image from *BT-20* class viewed at 20× magnification

problems associated with the use of cancer cell lines [26]. STR profiling is currently an international reference standard for identification of human cell lines. However, applying STR method takes a long time and an expert is required to carry out STR profiling. In addition, STR is a very costly process, necessitating efficient and rapid tools that can perform the task of cell identification in an automated manner. Computer-assisted identification of cancer cells can alleviate the burden of manual labeling, eliminate disadvantages of STR and thus facilitate cancer research. Figures 2.1 and 2.2 show sample human cancer cell line images of type *BT-20* and *MV*, respectively, acquired with Olympus CKX41 inverted microscope.

In this chapter, an image classification framework based on dual-tree complex wavelet transform (DT-CWT), directional difference scores and covariance features is proposed to automatically classify human cancer cell line images belonging to 14 different classes. Covariance descriptors obtained through the use of DT-CWT coefficients and directional difference scores are classified using the

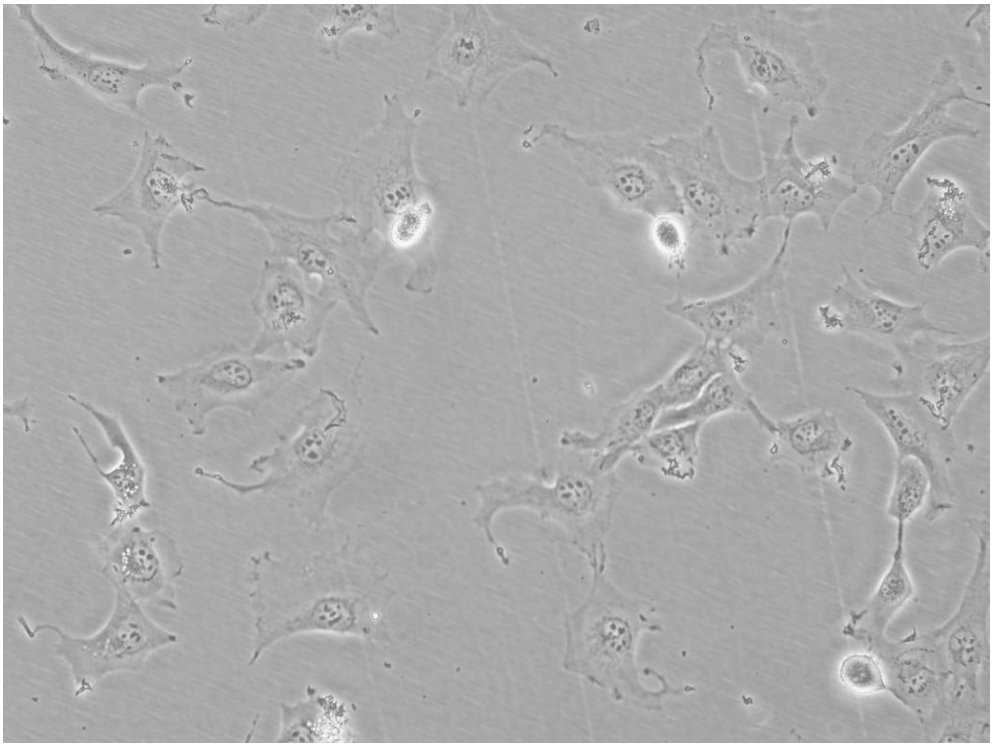

Figure 2.2: Sample cancer cell line image from MV class viewed at 20× magnification

multi-class Support Vector Machine (SVM) [27] classifier. The performance of the proposed algorithm is compared with the classical covariance descriptors.

The rest of the chapter is organized as follows. In Section 2.1, related work on cancer cell line classification in microscopic images is presented. Section 2.2 describes the image segmentation and subwindow selection procedure used in extracting regions-of-interest (ROIs) from cell line images. In Section 2.3, DT-CWT and covariance based feature extraction methods applied to human cancer cell line images are proposed. Classification strategy is described in Section 2.4. Cancer cell line image dataset used in the experimental studies is introduced in Section 2.5 and experimental results and observations are presented in Section 2.6. MATLAB$^{\text{TM}}$ R2012a computational environment is used for experimental studies and simulations.

2.1 Related Work on Cancer Cell Line Classification

Previous work on computerized identification of cancer cell lines is limited as STR analysis has become the standard way of checking the identity of cell lines in molecular biology community. Modelling of cell morphology has been studied by several groups, for example for fission yeast in [28] and for escherichia coli bacteria in [29]. In the fission yeast case, differential expression of protein affects the cell size and, therefore, cell fate, while in the escherichia coli case, the topological organization is analyzed with respect to the underlying signaling network. In [30], Bayesian classification algorithm exploiting the sparsity in a transform domain for differentiation of cell line images is proposed in which eigenvalues of the conventional covariance descriptor computed from fixed-size image blocks are used as features. We incorporate the complex wavelet transform into region covariance descriptors for feature extraction from microscopic images. In addition, a new set of features based on directional differences is proposed and used in covariance descriptors.

In Subsection 2.1.1, DT-CWT is briefly explained. Detailed description of DT-CWT based features is presented in Section 2.3. In Subsection 2.1.2, directional difference scores are proposed and explained. In Subsection 2.1.3, covariance and normalized covariance based methods are presented, which will be used in Section 2.3 for encoding complex wavelet subbands of cell line images.

2.1.1 Dual-Tree Complex Wavelet Transform

Wavelet theory has been providing a basis for many signal processing applications over the years. It has been introduced by the pioneering works of Daubechies [31], Mallat [32] and Grossman *et al.* [33]. Wavelets can be defined as dilated, translated and rotated versions of a locally oscillating prototype function, that are used to represent signals in both time and frequency domains at multiple decomposition levels. The discrete wavelet transform (DWT), which is aimed at processing

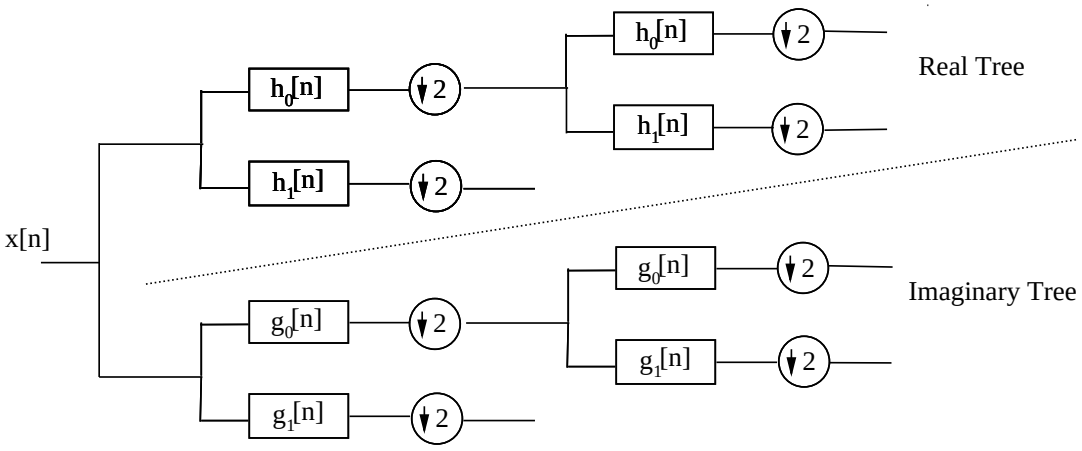

Figure 2.3: Filterbanks for the dual-tree complex wavelet transform

discrete-time signals, can be implemented using orthogonal or biorthogonal filterbanks and can be efficiently exploited for signal analysis. A computationally efficient implementation of the wavelet transform is provided by lifting structures [34]. Wavelets have proved useful in a broad range of applications, including image and video coding [35, 36], audio compression [37], speech recognition [38], texture classification and retrieval [39, 40] and denoising [41]. Recently, motion detection [42], and fire and flame detection [43] algorithms based on wavelet domain analysis of video were proposed.

The classical DWT has several limitations hampering its effectiveness in signal and image analysis, such as shift variance and lack of directionality [10]. When the input is shifted slightly, the discrete wavelet coefficients may change significantly. Higher dimensional DWT is implemented using separable filterbanks along each dimension and thus fails to capture directional information except at 0 and 90 degrees, for example, for a 2D DWT. To overcome such limitations of DWT, the dual-tree complex wavelet transform (DT-CWT) was proposed whereby two filter pairs are used in parallel to decompose a given signal [44].

DT-CWT has recently emerged as a promising alternative to the classical DWT in a variety of signal and image processing tasks including denoising [5], classification [6], texture analysis [7], compression [8] and watermarking [9]. DT-CWT has desirable properties such as shift invariance, directional selectivity and

lack of aliasing. In the dual-tree ℂWT, two maximally decimated DWTs are executed in parallel in a way that enables the wavelet functions of two different trees to form an approximate Hilbert transform pair [10]. These two wavelet trees are named real and imaginary trees, respectively. Low-pass analysis filters in real and imaginary trees must be offset by a half-sample in order to have one wavelet basis as the approximate Hilbert transform of the other wavelet basis [45]. Analyticity allows one-dimensional DT-CWT to be approximately shift-invariant and free of aliasing artifacts often encountered in DWT-based processing. Two-dimensional DT-CWT is also directionally selective in six different orientations, namely, $\{\pm 15, \pm 45, \pm 75\}$. Analysis filterbanks for one-dimensional DT-CWT are shown in Figure 2.3.

In the biomedical image analysis literature, DT-CWT is used to predict the histological diagnosis of colorectal lesions in colonoscopy images by employing a probabilistic framework where a joint statistical model for complex wavelet coefficient magnitudes is proposed [46]. In [47], authors model the marginal distributions of DT-CWT coefficient magnitudes by Rayleigh and Weibull probability density functions to classify the zoom-endoscopy images for colorectal cancer diagnosis. In [48], MR images of human brain and wrist are classified using textural features extracted via DT-CWT decomposition.

Cancer cell line images contain significant amount of oriented singularities. Attributes like orientation selectivity and shift invariance render DT-CWT a good choice for the processing of microscopic images with lots of edge- or ridge-like singularities. As a part of this thesis, microscopic cancer cell line images are represented in complex wavelet domain. It is explained in Section 2.3 how coefficients in this domain are exploited for cell line image analysis.

2.1.2 Directional Differences

In order to account for the large morphological variation of the images in our dataset, we evaluate differences between pixels in various directions. Inspired by

the local binary pattern (LBP) approach [49], a new directional feature computation approach is introduced for texture characterization. Consider a point p_1 on a two-dimensional function $I(x, y)$. Now consider a second point p_2. The Euclidean distance between p_1 and p_2 is d and p_2 lies on line that has an orientation of angle α with respect to the x-coordinate, i.e., p_2 lies on a circle whose center point is p_1 and has a radius d. The difference between p_1 and p_2 can be written as

$$T(d, \alpha) = |I(x, y) - I(x + d \cdot \cos\alpha, y + d \cdot \sin\alpha)| \tag{2.1}$$

Now consider we want to compute a couple of difference values for equidistant concentric circles where the largest circle has radius R and the smallest has radius R/A, where A is an integer with values ranging from $[1, R]$. When the parameters R and A are fixed, the equation (2.1) can be rewritten as

$$T(i, \alpha) = \left| I(x, y) - I(x + i\frac{R}{A} \cdot \cos\alpha, y + i\frac{R}{A} \cdot \sin\alpha) \right| \tag{2.2}$$

where $i \in 1, 2, ..., A$. We can compute a score for each α value by computing a function with respect to i, as

$$s_\alpha = \mathcal{F}_i(T(i, \alpha)) \tag{2.3}$$

In this thesis, $\mathcal{F}_i$ is chosen to be the median function. In that case, s_α is simply the median of all the differences between the center pixel and the points at distances $i\frac{R}{A}$ at the fixed orientation α. s_α is computed for each pixel of the image and these scores are used as features in covariance matrix computation. For each input image, eight output images of the same size are generated as the result of the function $\mathcal{F}_i$, corresponding to 8 different orientations when the radius d is chosen as 5 in the experiments. In Section 2.3, directional difference scores are used in covariance descriptors for cancer cell line image analysis.

2.1.3 Covariance Descriptor

Region covariance provides a powerful descriptor for representing image regions, which was proposed by Tuzel *et al.* [50]. It has attained a great deal of interest

from computer vision community. Covariance descriptors enable the combination of different features over an image region of interest. In the region covariance framework each pixel is mapped to a set of pixel properties whose variances and correlations with one another are utilized in a covariance matrix as region descriptor. Given an intensity image I of size $m \times n$, we define a mapping ϕ from image domain to feature domain as

$$F(i,j) = \phi(I,i,j) \tag{2.4}$$

where each pixel (i,j) in I is mapped to a set of features and F is the $m \times n \times d$ dimensional feature function. Let $f_{i,j}, 1 \leq i \leq m, 1 \leq j \leq n$, be the d-dimensional feature vectors extracted for the $(i,j)^{th}$ pixel of the image. Then, the covariance matrix of the image I can be computed as

$$C = \frac{1}{N-1} \sum_{i=1}^{m} \sum_{j=1}^{n} (f_{i,j} - \mu)(f_{i,j} - \mu)^T \tag{2.5}$$

where $N = m \times n$ and μ is the mean of the feature vectors inside the region I, which can be calculated as

$$\mu = \frac{1}{N} \sum_{i=1}^{m} \sum_{j=1}^{n} f_{i,j} \tag{2.6}$$

The covariance matrix is symmetric positive-definite and of size $d \times d$. There exists a very efficient multiplier-less implementation of covariance descriptors, called co-difference matrices, which have been shown to yield comparable performances to the original ones [51].

In [50], covariance features are employed for object detection and texture classification tasks. Each object region is represented by five overlapping subregions and a covariance matrix is constructed from each subregion. Pixel features used in constructing covariance matrices include pixel x and y coordinates, R, G and B values from the RGB space, first and second derivatives of the image intensity in both x and y directions. Desired object locations are determined in the target image by executing an exhaustive search, where generalized eigenvalue-based dissimilarity measure is employed to compute the distance between covariance

matrices. In [52], pedestrian detection is achieved by encoding positive and negative pedestrian regions via covariance descriptors. Spatio-temporal covariance descriptors representing spatio-temporal blocks of video are proposed in [53] for flame detection. [54] uses covariance features to describe one-dimensional speech signals for speech emotion classification. Covariance descriptors are utilized for classification of colonic polyps in CT colonography images [55].

Feature vectors extracted from each pixel must be selected taking into account the specific properties of the application domain. It may be adequate to use image intensity, color values and derivatives in x and y directions in detection tasks such as object detection, pedestrian detection and flame detection, whereas biomedical images require more sophisticated approaches that can encode ROI's in a discriminative manner. Feature vectors used in this thesis will be detailed in Section 2.3.

2.2 Image Segmentation and Subwindow Selection

In this chapter, ROI extraction process from cancer cell line images is described. First, image segmentation is performed to obtain cellular regions and then ROI's are selected from foreground cellular regions.

The images in our dataset exhibit a large amount of background. Clearly, the background is not discriminative. Therefore, we address the issue of segmenting the images into foreground and background before calculation of covariance matrices from image patches. For our dataset, a simple thresholding scheme like Otsu's method [56] does not provide satisfactory segmentation results, since foreground pixels have a large variance and may therefore have values higher and lower than the background pixels. Hence, the distribution of cellular and background components is modeled using a Gaussian mixture model. The mixture parameters $\mathbf{\Theta} = (\alpha_F, \alpha_B, \mu_F, \mu_B, \sigma_F, \sigma_B)$ are estimated using the expectation maximization (EM) algorithm [57], where α_F, μ_F, σ_F and α_B, μ_B, σ_B are mixing weights,

mean and variance of the distributions of foreground and background pixels, respectively. EM is an iterative algorithm that obtains the maximum likelihood estimates of distribution parameters using training samples. This is achieved by assuming the existence of additional hidden parameters. In the expectation step, the expectation of the complete-data log-likelihood is calculated with respect to the hidden data y given the observations x and the current estimates $\mathbf{\Theta}^{(i-1)}$ as follows:

$$Q(\mathbf{\Theta}, \mathbf{\Theta}^{(i-1)}) = E[log\ p(x, y|\mathbf{\Theta})|x, \mathbf{\Theta}^{(i-1)}] \tag{2.7}$$

where x denotes pixel values and y denotes the mixture component that generates the pixel value. In the maximization step, a new parameter set $\mathbf{\Theta}$ is determined that maximizes the expectation in Equation (2.7):

$$\mathbf{\Theta}^{(i)} = \arg\max_{\mathbf{\Theta}} Q(\mathbf{\Theta}, \mathbf{\Theta}^{(i-1)}) \tag{2.8}$$

After the parameter estimation process is finished, the posterior probability of each pixel x can be computed as

$$p(c_i|x) = \frac{\alpha_i p(x|c_i) P(c_i)}{\sum_j \alpha_j p(x|c_j) P(c_j)}, \tag{2.9}$$

where i denotes foreground or background components and $p(x|c_i) = N(x; \mu_i, \sigma_i)$ is the value of the Gaussian distribution parametrized by the mean and variance of the corresponding component. For segmentation, x is assigned to the component that yields the higher posterior probability.

The resulting image obtained by EM segmentation of the image in Figure 2.1 is shown in Figure 2.4(a). As can be seen from the result, the image is noisy. Hence, a morphological closing operation is applied, followed by median filtering. Figure 2.4(b) illustrates the final image mask obtained after closing and median filtering.

Once the foreground cellular regions are identified via segmentation, ROI's can be selected from those regions. Since cancer cell line images contain lots of flat, background-like regions, it is not reasonable to compute the covariance matrix over the whole image region. Exclusion of background regions in covariance

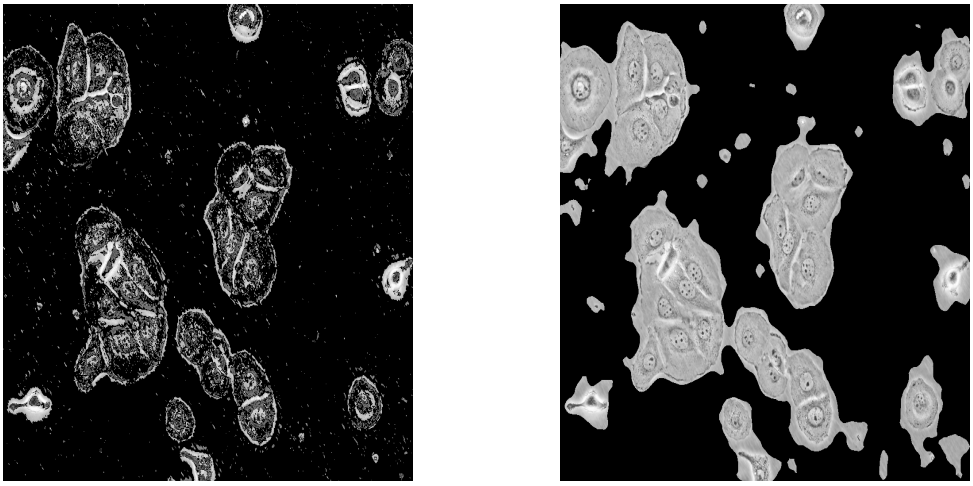

(a) EM segmentation

(b) EM segmentation followed by closing and median filtering

Figure 2.4: Image masks obtained (a) after EM segmentation and (b) after closing and median filtering on top of EM output using the image in Figure 2.1

computation helps to increase the class separability in classification. We propose to use random subwindow selection method for cancer cell line images [58]. Each image is represented by possibly overlapping s square subwindows selected at random locations and with random edge lengths. The edge length of the largest possible subwindow is equal to that of the shorter edge of the image, while the size of the smallest possible subwindow is 10 times lower than that of the largest one. We enforce a foreground percentage constraint on the selected subwindows to avoid gathering background regions. A randomly chosen subwindow is discarded, if its foreground percentage is below a threshold, which is determined to be 50%. Random window selection process continues until the total number of windows becomes s. We compute a covariance matrix for each subwindow and an image is represented by s covariance matrices. Random subwindow selection process is illustrated in Figure 2.5 for a sample cancer cell line image. Random sampling approach avoids the need to scan the whole image to regularly take samples, which is computationally expensive, and provides scale-invariance of analysis windows by considering cells of any size for processing.

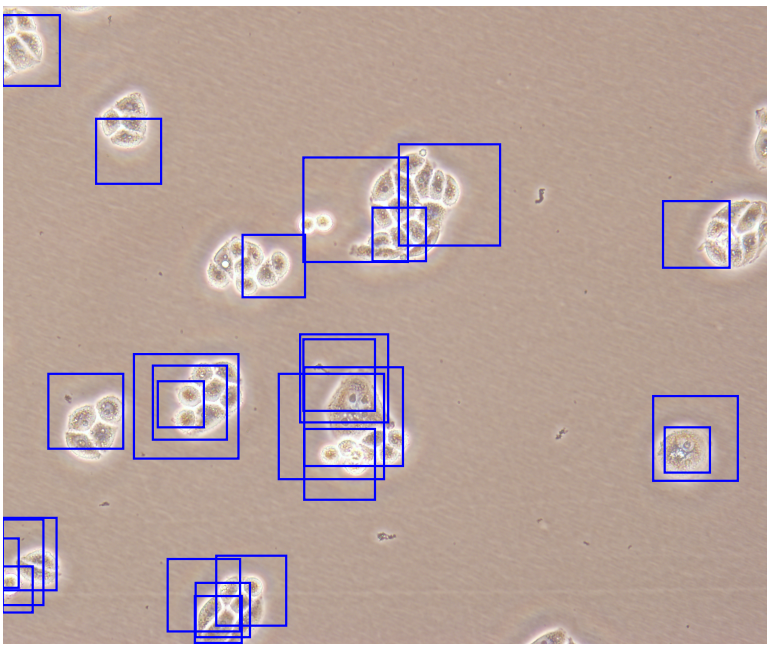

Figure 2.5: Random subwindow selection process on a sample cancer cell line image

2.3 DT-CWT and Covariance Based Feature Extraction

In this section, DT-CWT based feature extraction technique that employs covariance descriptors is proposed for cancer cell line images. DT-CWT is a recently developed image decomposition method that possesses orientation selectivity and shift invariance properties lacking in the classical DWT. In the literature, it was used for texture analysis and classification, video compression and image watermarking [6, 7, 8, 9].

In contrast to the real DWT, two sets of filters are employed in the two trees, which are called real and imaginary trees, respectively. Two different DWTs are executed in parallel in dual-tree structure where the real part of DT-CWT is provided by the first one and the imaginary part by the second one. The reasoning behind the use of dual-tree is to obtain an analytic complex wavelet at

the end:

$$\psi_c(t) = \psi_h(t) + j\psi_g(t) \tag{2.10}$$

where $\psi_h(t)$ and $\psi_g(t)$ denote wavelet functions of real and imaginary trees, respectively. If $\psi_c(t)$ is approximately analytic (has support on only one-side of the frequency axis), the resulting transform can possess the properties such as lack of aliasing, directionality and shift invariance just like the Fourier transform whose complex basis functions are analytic [10]. For $\psi_c(t)$ to be approximately analytic, it is required that one wavelet basis is the approximate Hilbert transform of the other wavelet basis:

$$\psi_g(t) \approx \mathcal{H}\{\psi_h(t)\} \tag{2.11}$$

In order to satisfy the condition in (2.11), low-pass analysis filters in real and imaginary trees must be offset approximately by half-sample [45]:

$$g_0[n] \approx h_0[n - 0.5] \tag{2.12}$$

In the literature, two low-pass filters are jointly designed such that half-sample delay, perfect reconstruction and finite support conditions are simultaneously satisfied, using several filter design methods [10]. Q-shift filters are employed in this thesis for DT-CWT decomposition. Analysis q-shift filters for real and imaginary trees are shown in Table 2.1 [59].

Analysis filters	h_0	h_1	g_0	g_1
Q-shift filter coefficients	0.0248	-0.0808	-0.0808	-0.0248
	0	0	0	0
	-0.0624	0.4155	0.4155	0.0624
	0.1653	-0.5376	0.5376	0.1653
	0.5376	0.1653	0.1653	-0.5376
	0.4155	0.0624	-0.0624	0.4155
	0	0	0	0
	-0.0808	-0.0248	0.0248	-0.0808

Table 2.1: Impulse Response of Kingsbury's 8^{th} Order Q-shift Analysis Filters for the Dual-Tree $\mathbb{C}$WT

Two-dimensional (2D) extension of DT-CWT is used for analysis of cancer cell line images. 2D DT-CWT of an image is obtained by four real separable transforms [60]. Real-part and imaginary-part analysis filters are applied successively

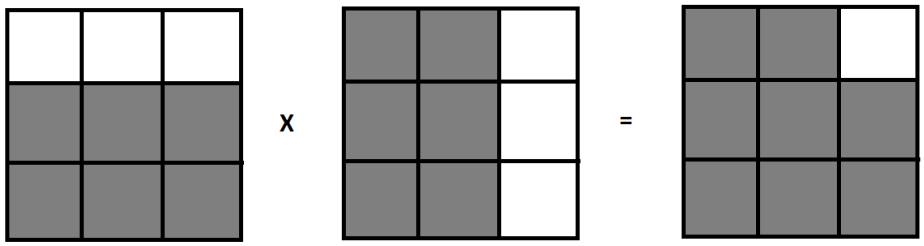

Figure 2.6: 2D analytic complex wavelet obtained from two 1D analytic complex wavelets

to rows and columns of the image. Implementation details for 2D DT-CWT [10] are as follows. Let $\psi(x) = \psi_h(x) + j\psi_g(x)$ denote an approximately analytic complex wavelet in the Fourier domain. The 2D separable wavelet $\psi(x, y) = \psi(x)\psi(y)$ obtained by row-column implementation can be expressed as

$$\psi(x, y) = [\psi_h(x) + j\psi_g(x)][\psi_h(y) + j\psi_g(y)] \tag{2.13}$$

$$= \psi_h(x)\psi_h(y) - \psi_g(x)\psi_g(y) + j[\psi_g(x)\psi_h(y) + \psi_h(x)\psi_g(y)] \tag{2.14}$$

Since $\psi(x)$ is analytic, it is supported only on one side of the frequency axis. Hence, the multiplication of these two analytic wavelets results in a 2D complex wavelet that has support only on one quadrant of the 2D frequency domain. This process is illustrated in Figure 2.6, in which boxes represent 2D Fourier domain idealized diagrams of the wavelet functions where the functions are supported on white regions and have no support on black regions. The real part of this 2D complex wavelet is given by

$$\Re\{\psi(x, y)\} = \psi_h(x)\psi_h(y) - \psi_g(x)\psi_g(y) \tag{2.15}$$

which is implemented by taking the difference of high-pass subbands of the real and imaginary trees in a separable row-column processing.

Real wavelets should be symmetric with respect to the origin; hence, taking the real part of the resulting spectrum in Figure 2.6 yields the 2D real oriented wavelet as shown in Figure 2.7. It highlights image structures oriented at 45^o, and thus is oriented at -45^o. The real part of the 2D complex wavelet $\psi_2(x, y) = \psi(x)\overline{\psi(y)}$ yields a 2D wavelet oriented at 45^o since taking the conjugate would

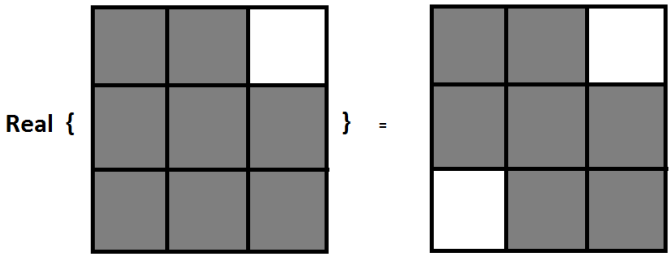

Figure 2.7: Oriented 2D wavelet given by the real part of the analytic 2D wavelet

move the support to the left side of the frequency plane, thereby generating a 2D complex wavelet supported only on the 2^{nd} quadrant of the plane similar to the procedure in Figure 2.6. For other four orientations, the following four complex 2D wavelets should be employed: $\phi(x)\psi(y)$, $\psi(x)\phi(y)$, $\phi(x)\overline{\psi(y)}$, and $\psi(x)\overline{\phi(y)}$. If the aforementioned procedure is repeated by taking imaginary parts of the 2D complex wavelets instead of real parts, six real and imaginary orientations, $\{\pm 15, \pm 45, \pm 75\}$, are obtained. 2D DT-CWT implementation scheme is shown in Figure 2.8. As seen from the figure, four separable transforms, F_{HH}, F_{HG}, F_{GH}, F_{GG}, are executed in parallel for 2D DT-CWT decomposition, where F_{AB} denotes row-column separable transform with the filterbank A used for row processing and the filterbank B used for column processing.

The 1^{st} level 2D DT-CWT subbands are obtained by taking the sum and difference of respective subbands shown at the output of filterbanks in Figure 2.8. Twelve 2D DT-CWT detail subband images are computed as follows:

$$d_{1,2} = x_{h_0h_1} \pm x_{g_0g_1} \tag{2.16}$$

$$d_{3,4} = x_{h_1h_0} \pm x_{g_1g_0} \tag{2.17}$$

$$d_{5,6} = x_{h_1h_1} \pm x_{g_1g_1} \tag{2.18}$$

$$d_{7,8} = x_{g_0h_1} \pm x_{h_0g_1} \tag{2.19}$$

$$d_{9,10} = x_{g_1h_0} \pm x_{h_1g_0} \tag{2.20}$$

$$d_{11,12} = x_{g_1h_1} \pm x_{h_1g_1} \tag{2.21}$$

where each of the six orientations corresponds to two detail subbands, one of them being real and another being imaginary. Low-pass subbands, $x_{h_0h_0}$, $x_{h_0g_0}$, $x_{g_0h_0}$ and $x_{g_0g_0}$, are fed to the next level row filters for further processing at higher

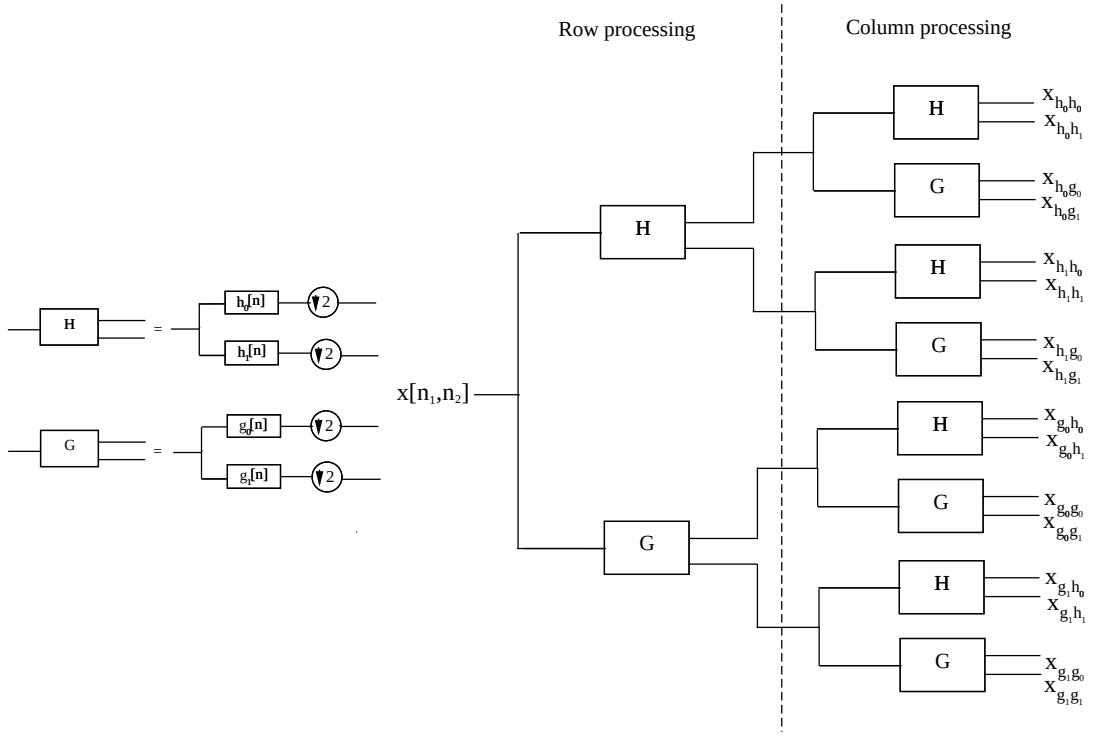

Figure 2.8: Implementation scheme of the 2D DT-CWT. Four real separable DWT's are employed in 2D DT-CWT.

decomposition levels. At each decomposition level, we obtain a total of sixteen subbands consisting of six real detail subbands, six imaginary detail subbands and four approximation subbands. Two-dimensional dual-tree decomposition is an oversampled transform with a redundancy factor of 4 (2^d for d-dimensional signals). A sample image and its 2^{nd} level 2D DT-CWT subbands are shown in Figures 2.9 and 2.10, respectively. In Figure 2.10, the first row contains the approximation subbands and the remaining rows contain the detail subbands at six different orientations. In our work, we perform three-level 2D DT-CWT decomposition of each biomedical image of size $m \times n$ and use the detail subband coefficients. Each subband at the i^{th} level is of size $m/2^i \times n/2^i$. The original image $I(x, y)$ is decimated by 8 in both directions to obtain a single intensity image $I_a(x, y)$ which represents the original image. Let $W_\theta^{R,(i)}(x, y)$ and $W_\theta^{Im,(i)}(x, y)$ denote, respectively, the real and imaginary part of the i^{th} level complex wavelet coefficient at the position (x, y) corresponding to directional detail subbands at orientation θ, where $\theta \in \{\pm 15, \pm 45, \pm 75\}$. The magnitude of the complex wavelet

coefficient is then given by

$$M_{\theta}^{(i)}(x,y) = \sqrt{W_{\theta}^{R,(i)}(x,y)^2 + W_{\theta}^{Im,(i)}(x,y)^2} \tag{2.22}$$

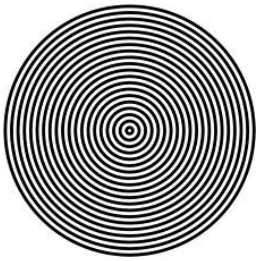

Figure 2.9: Sample image.

In this thesis, covariance descriptors are utilized to encode cancer cell line image windows in complex wavelet domain. Complex wavelet coefficient magnitudes in detail subbands are used as pixel features in covariance computation. Conventional covariance approach includes only gray-scale and color values, and their derivatives in horizontal and vertical directions, which limits the discriminatory power of the covariance representation. Augmenting covariance matrices with directional information through the use of 2D DT-CWT may help to enhance the classification accuracy. Directional difference scores introduced in Subsection 2.1.2 are also included in the feature vectors.

Intensity value, first and second order derivatives in horizontal and vertical directions are also included in the feature vector in addition to DT-CWT and directional difference features. 1^{st}, 2^{nd} and 3^{rd} level DT-CWT coefficients are tested to observe the effect of decomposition level on classification performance. With

$$\mathbf{M}_{\theta}^{(\mathbf{i})}(\mathbf{x},\mathbf{y}) = [M_{\theta_1}^{(i)}(x,y)...M_{\theta_6}^{(i)}(x,y)], \tag{2.23}$$

and

$$\mathbf{s}_{\alpha}(\mathbf{x},\mathbf{y}) = [s_{\alpha_1}(x,y) \ ... \ s_{\alpha_8}(x,y)] \tag{2.24}$$

where $\theta_1...\theta_6$ corresponds to the six orientations of DT-CWT detail subbands

$\{\pm 15, \pm 45, \pm 75\}$, $M_\theta^{(i)}(x,y)$ is as defined in Equation (2.22) and $\alpha_1 ... \alpha_8$ correspond to the eight orientations of directional difference score estimation, the following feature mapping functions are employed to compute covariance matrices:

$$\phi_1(I,x,y) = \left[I_a(x,y) \ \left|\frac{\partial I_a}{\partial x}\right| \ \left|\frac{\partial I_a}{\partial y}\right| \ \left|\frac{\partial^2 I_a}{\partial x^2}\right| \ \left|\frac{\partial^2 I_a}{\partial y^2}\right| \right]^T \tag{2.25}$$

$$\phi_2(I,x,y) = \left[I_a(x,y) \ \mathbf{M}_\theta^{(\mathbf{1})}(\mathbf{x},\mathbf{y}) \right]^T \tag{2.26}$$

$$\phi_3(I,x,y) = \left[I_a(x,y) \ \left|\frac{\partial I_a}{\partial x}\right| \ \left|\frac{\partial I_a}{\partial y}\right| \ \left|\frac{\partial^2 I_a}{\partial x^2}\right| \ \left|\frac{\partial^2 I_a}{\partial y^2}\right| \ \mathbf{M}_\theta^{(\mathbf{1})}(\mathbf{x},\mathbf{y}) \right]^T \tag{2.27}$$

$$\phi_4(I,x,y) = \left[I_a(x,y) \ \left|\frac{\partial I_a}{\partial x}\right| \ \left|\frac{\partial I_a}{\partial y}\right| \ \left|\frac{\partial^2 I_a}{\partial x^2}\right| \ \left|\frac{\partial^2 I_a}{\partial y^2}\right| \ \mathbf{M}_\theta^{(\mathbf{1})}(\mathbf{x},\mathbf{y}) \ \mathbf{s}_\alpha(\mathbf{x},\mathbf{y}) \right]^T \tag{2.28}$$

$$\phi_5(I,x,y) = \left[I_a(x,y) \ \mathbf{M}_\theta^{(\mathbf{2})}(\mathbf{x},\mathbf{y}) \right]^T \tag{2.29}$$

$$\phi_6(I,x,y) = \left[I_a(x,y) \ \left|\frac{\partial I_a}{\partial x}\right| \ \left|\frac{\partial I_a}{\partial y}\right| \ \left|\frac{\partial^2 I_a}{\partial x^2}\right| \ \left|\frac{\partial^2 I_a}{\partial y^2}\right| \ \mathbf{M}_\theta^{(\mathbf{2})}(\mathbf{x},\mathbf{y}) \right]^T \tag{2.30}$$

$$\phi_7(I,x,y) = \left[I_a(x,y) \ \left|\frac{\partial I_a}{\partial x}\right| \ \left|\frac{\partial I_a}{\partial y}\right| \ \left|\frac{\partial^2 I_a}{\partial x^2}\right| \ \left|\frac{\partial^2 I_a}{\partial y^2}\right| \ \mathbf{M}_\theta^{(\mathbf{2})}(\mathbf{x},\mathbf{y}) \ \mathbf{s}_\alpha(\mathbf{x},\mathbf{y}) \right]^T \tag{2.31}$$

$$\phi_8(I,x,y) = \left[I_a(x,y) \ \mathbf{M}_\theta^{(\mathbf{3})}(\mathbf{x},\mathbf{y}) \right]^T \tag{2.32}$$

$$\phi_9(I,x,y) = \left[I_a(x,y) \ \left|\frac{\partial I_a}{\partial x}\right| \ \left|\frac{\partial I_a}{\partial y}\right| \ \left|\frac{\partial^2 I_a}{\partial x^2}\right| \ \left|\frac{\partial^2 I_a}{\partial y^2}\right| \ \mathbf{M}_\theta^{(\mathbf{3})}(\mathbf{x},\mathbf{y}) \right]^T \tag{2.33}$$

$$\phi_{10}(I,x,y) = \left[I_a(x,y) \ \left|\frac{\partial I_a}{\partial x}\right| \ \left|\frac{\partial I_a}{\partial y}\right| \ \left|\frac{\partial^2 I_a}{\partial x^2}\right| \ \left|\frac{\partial^2 I_a}{\partial y^2}\right| \ \mathbf{M}_\theta^{(\mathbf{3})}(\mathbf{x},\mathbf{y}) \ \mathbf{s}_\alpha(\mathbf{x},\mathbf{y}) \right]^T \tag{2.34}$$

where the first and second order intensity derivatives are calculated using the filters $[-1, 0, 1]$ and $[1, -2, 1]$, respectively. Sizes of the covariance matrices obtained by using the above feature vectors are shown in Table 2.2. ϕ_1 is used to evaluate the performance of the conventional covariance descriptors including only intensity and color values and their derivatives, as in [11, 61]. The 1^{st} level DT-CWT coefficient magnitudes in detail subbands are tested in ϕ_2, ϕ_3 and ϕ_4, with intensity, first and second order intensity derivatives and directional difference scores, respectively. The effect of the 2^{nd} and 3^{rd} level DT-CWT coefficients are tested in the remaining feature vectors.

Covariance matrices are calculated for each subwindow of the image as extracted in Section 2.2. [11] proposes to use the generalized eigenvalue based

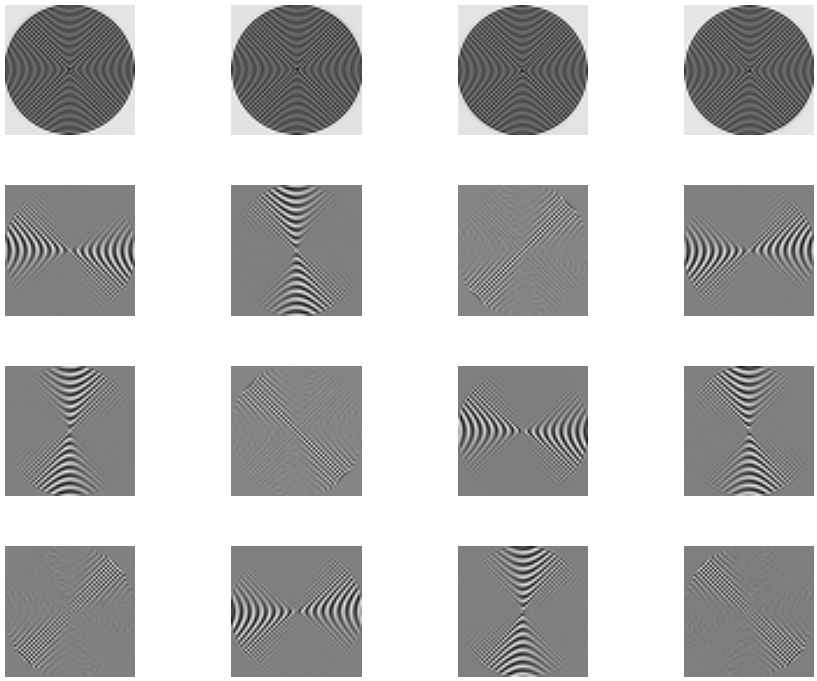

Figure 2.10: Second level 2D DT-CWT subbands of the image in Figure 2.9

distance metric for calculating the dissimilarity of two covariance matrices as the Euclidean distance is meaningless for covariance matrices, which do not lie in Euclidean space. Kullback-Leibler (KL) divergence is used in [62] for comparing covariance matrices. However, both distance metrics are computationally expensive and require an extensive amount of time for distance calculation in huge datasets, as is the case with our dataset. Therefore, covariance matrices are vectorized and classified in the resulting feature space using SVM [61]. We adopt the vectorization approach and include only the upper or lower diagonal elements of the covariance matrix in classification.

In [63], normalized covariance descriptors are introduced and utilized for real-time wildfire detection. We also test the normalized covariance matrices in cancer cell line classification. Each entry $\hat{C}(i,j)$ of a normalized covariance matrix is

Table 2.2: Sizes of the Covariance Matrices Used

Mapping Function	ϕ_1	ϕ_2	ϕ_3	ϕ_4	ϕ_5	ϕ_6	ϕ_7	ϕ_8	ϕ_9	ϕ_{10}
Matrix Size	5×5	7×7	11×11	19×19	7×7	11×11	19×19	7×7	11×11	19×19

obtained from the covariance matrix C as follows:

$$\hat{C}(i,j) = \begin{cases} \sqrt{C(i,j)}, & \text{if } i = j \\ \frac{C(i,j)}{\sqrt{C(i,i)C(j,j)}}, & \text{otherwise} \end{cases} \tag{2.35}$$

2.4 Classification Algorithm

For each subwindow sampled from images as explained in Section 2.2, a covariance matrix is computed using Equation (2.5) for each of the feature mapping functions in (2.25)-(2.34). The image signature is composed of s covariance matrices of the same size. Each class is represented by $s \times \#$(images in each class) covariance matrices. Covariance matrices are symmetric positive-definite and do not lie in the Euclidean space; so, they are vectorized resulting in $d(d+1)/2$-dimensional feature vectors for $d \times d$ matrices. Proposed by Boser *et al.* [64], SVM is a supervised machine learning algorithm that learns the decision boundaries between classes using separating hyperplanes. LIBSVM library [27] is used for SVM implementation. A multiclass SVM classifier is trained with RBF kernel in the $d(d+1)/2$-dimensional vector space using the training points. For each test subwindow, the corresponding covariance descriptor is vectorized and fed into the trained SVM model for prediction. Therefore, there exist s labels for each microscopic image corresponding to s subwindows, and the image in question is assigned the label that gets the majority of votes among s labels. The above process is re-executed using normalized covariance matrices defined in Equation (2.35) instead of covariance matrices.

2.5 Cancer Cell Line Image Dataset

The dataset used in this study consists of 280 microscopic human carcinoma cell line images with each of the 14 classes having 20 images. Images in the dataset were acquired at 10x, 20x and 40x magnifications; thus, we have a total of 840 images in the dataset. The size of each image is 3096×4140 pixels. 7 classes belong to breast cancer cell lines and the other classes belong to liver cancer. Each cell type has a specific phenotype in terms of nuclei (spherical vs. ovoid), nucleoli (prominent vs. hardly noticeable), size (large vs. small) and shape (round vs. cell pods) [65]. The names of the cancer cell lines used in our study are shown in Table 2.3. Aggressive cancer cells with metastatic properties switch from an epithelial-like (epithelioid) morphology to a spindle-shaped fibroblast-like (fibroblastoid) morphology during epithelial-mesenchymal transition (EMT), which is an indication of the invasiveness and metastatic capability of cancer cells. While epithelioid cells have polygonal shape with regular dimensions and sharp boundaries, fibroblastoid cells have elongated shapes and are bipolar or multipolar.

Table 2.3: Names of Cancer Cell Lines Used in This Study

Breast cancer cell line	Liver cancer cell line
BT-20	Focus
Cama-1	Hep40
MDA-MB-157	HepG2
MDA-MB-361	Huh7
MDA-MB-453	MV
MDA-MB-468	PLC
T47D	SkHep1

6 hepatocellular carcinoma (Focus, Hep40, Huh7, Mahlavu, PLC, SkHep1), 1 hepatoblastoma (HepG2) and 7 breast cancer (Cama-1, MDA-MB-157, MDA-MB-361, MDA-MB-453, MDA-MB-468, T47D, BT-20) cell lines were seeded into dishes with 20% confluency and grown at 37^{o}C under 5% CO_2 in standard Dulbecco's modified Eagle's medium (DMEM) supplemented with 10% FBS, 1%

Non-Essential Aminoacid and 1% penicillin/streptomycin (GIBCO Invitrogen) up to 70% confluency. The cell lines used in this study were original and verified by STR analysis. Pictures were taken with Olympus CKX41 inverted microscope using Olympus DP72 camera with 10x, 20x and 40x objective.

2.6 Experimental Results

Feature vectors extracted via DT-CWT decomposition and covariance matrices are experimented on the cancer cell line image dataset mentioned in Section 2.5. We adopt a 20-fold cross-validation strategy for the experiments. The dataset is divided into 20 disjoint subsets and each subset consisting of 14 images is used exactly once as the test set. For $k = 1...20$, the k^{th} subset is formed by taking the k^{th} indexed image of each class. We run 20 experiments, choosing each image as the test image only once for each class, and obtain the average image classification accuracy over 20 runs. The number of selected random subwindows is taken to be $s = 100$. The above experiment is performed for both covariance and normalized covariance matrices, and for ten different mapping functions in (2.25)-(2.34). Separate experiments are carried out for three different datasets associated with the magnification factors 10x, 20x and 40x, respectively.

Experimental results are presented on three different tables corresponding to three different magnifications. Both image classification accuracies and subwindow classification accuracies are shown on tables. Subwindow accuracies are computed for the sole purpose of obtaining the intermediate results; what is important is the accuracy of classification on an image level which is accomplished by majority voting among the selected subwindows. Tables 2.4-2.6 present overall image and subwindow classification accuracies of 14 different classes over the cancer cell line image datasets at 10x, 20x and 40x magnifications, respectively. The highest image accuracy in each of these tables is highlighted in bold.

The experiments indicate that the normalized covariance matrices are more

Table 2.4: Overall Image and Subwindow Classification Accuracies in (%) of the Covariance and Normalized Covariance Methods for 10x Cancer Cell Line Image Dataset

Feature Mapping Function	Covariance Method		Normalized Covariance Method	
	Image Accuracy	Subwindow Accuracy	Image Accuracy	Subwindow Accuracy
ϕ_1	89.6	59.6	90.4	61.0
ϕ_2	83.2	55.8	88.9	59.1
ϕ_3	94.6	68.0	95.4	68.0
ϕ_4	97.5	70.6	98.2	74.1
ϕ_5	82.1	55.3	87.9	59.3
ϕ_6	96.1	68.6	96.8	69.4
ϕ_7	96.8	70.1	98.6	75.0
ϕ_8	81.8	55.1	86.4	59.3
ϕ_9	95.7	68.8	96.8	69.4
ϕ_{10}	96.8	71.1	**98.9**	75.0

discriminative than the classical covariance matrices as both the image and subwindow classification accuracies improve in almost all cases when normalization is performed. The best overall image recognition rates for 10x, 20x and 40x datasets are 98.9%, 97.5% and 96.4%, respectively, all obtained by normalized covariance method.

For all the magnification factors, the feature mapping function ϕ_{10} containing 19 features leads to the highest image classification accuracy. It includes the 3^{rd} level DT-CWT detail subband complex coefficient magnitudes and directional difference scores in addition to intensity and intensity derivatives. It is observed that ϕ_4 and ϕ_7, which include 1^{st} and 2^{nd} level DT-CWT coefficients, respectively, as the only difference from ϕ_{10} are the best or the second best functions in all datasets. This shows that discriminative ability of the covariance descriptor increases as more features are included in the feature vector from which the covariance matrices are constructed. For instance, ϕ_2 is a subset of ϕ_3, which is a subset of ϕ_4; when intensity derivatives and directional difference scores are sequentially added to the feature vector, the algorithm becomes more accurate. However, the effect of DT-CWT decomposition level on classification performance is not pronounced since the accuracy of image classification only slightly differs among feature mapping functions corresponding to different DT-CWT levels such

Table 2.5: Overall Image and Subwindow Classification Accuracies in (%) of the Covariance and Normalized Covariance Methods for 20x Cancer Cell Line Image Dataset

Feature Mapping Function	Covariance Method		Normalized Covariance Method	
	Image Accuracy	Subwindow Accuracy	Image Accuracy	Subwindow Accuracy
ϕ_1	86.8	58.9	87.9	60.3
ϕ_2	82.1	56.3	90.4	60.3
ϕ_3	92.1	68.1	93.9	68.9
ϕ_4	95.7	71.5	**97.5**	74.6
ϕ_5	82.9	56.3	88.9	59.6
ϕ_6	91.8	68.9	96.1	70.0
ϕ_7	96.1	72.0	**97.5**	74.9
ϕ_8	82.9	56.4	89.3	59.9
ϕ_9	91.8	68.7	96.1	70.1
ϕ_{10}	96.4	72.0	**97.5**	75.0

as ϕ_2, ϕ_5 and ϕ_8.

Conventional covariance method represented by ϕ_1 is generally outperformed by DT-CWT based covariance descriptors ϕ_2, ϕ_3, ϕ_5, ϕ_6, ϕ_8 and ϕ_9. Directional information is embedded into covariance representation by the use of subband coefficients of DT-CWT, which possesses orientation selectivity. The experimental results demonstrate that classical covariance descriptors fail to capture the textural characteristics of cancer cell line images and result in unsatisfactory classification performance, whereas the proposed DT-CWT based covariance approach is well suited for the task of recognizing human cancer cell line images. Exploitation of directional information at six different orientations through the use of DT-CWT boosts the image recognition accuracy. Approximate shift invariance property of DT-CWT also adds a certain level of robustness to feature extraction step since it is capable of accurately localizing singularities without causing undesirable positive and negative oscillations around them.

The length of the feature vector corresponding to ϕ_{10}, which achieves the highest success rate, is $19 \times 20/2 = 190$, as seen from Table 2.2. 66-length feature vector of ϕ_9 leads to an accuracy of 96.8% for 10x dataset, causing 2.1% performance reduction. Hence, depending on the type of application, either the

Table 2.6: Overall Image and Subwindow Classification Accuracies in (%) of the Covariance and Normalized Covariance Methods for 40x Cancer Cell Line Image Dataset

Feature Mapping Function	Covariance Method		Normalized Covariance Method	
	Image Accuracy	Subwindow Accuracy	Image Accuracy	Subwindow Accuracy
ϕ_1	73.9	51.3	81.8	52.7
ϕ_2	71.8	50.2	81.8	56.7
ϕ_3	89.3	62.4	92.9	65.5
ϕ_4	92.5	64.9	**96.4**	70.3
ϕ_5	72.9	50.7	90	60.7
ϕ_6	89.3	63.8	92.9	67.1
ϕ_7	92.9	65.3	95.7	71.4
ϕ_8	73.2	50.9	90.4	60.8
ϕ_9	88.6	63.8	93.2	67.2
ϕ_{10}	92.9	65.4	**96.4**	71.6

classification accuracy or the speed of the algorithm must be compromised. It takes approximately 20 seconds to classify a cancer cell line image acquired at 20x magnification with a MATLAB implementation using ϕ_{10}, where the computation of directional difference scores lasts 8 seconds. Utilizing ϕ_9 instead of ϕ_{10} for feature extraction provides 8 seconds improvement in speed while degrading the accuracy by 2%. With a C++ implementation, average image classification time for both cases can drop below a second, which suggests that real-time application is possible. If the biologist that will use the developed system prioritizes speed (accuracy), the functions ϕ_3, ϕ_6 or ϕ_9 (ϕ_4, ϕ_7 or ϕ_{10}) can be preferred for feature computations.

Experimental results in Tables 2.4-2.6 indicate that the proposed cancer cell line image recognition algorithm provides promising classification accuracies and can be used as a reliable decision maker for laboratory studies. Based on the magnification at which the cell line images are acquired, the best feature vector can be selected by taking into account the trade-off between speed and accuracy of the resulting algorithm.

2.7 Summary

The proposed automated system for human breast and liver cancer cell line images can aid the biologist as a second reader and avoid the need for costly and time-consuming biochemical tests. Our approach aims to carry out the automated analysis by extracting a feature vector from the images. DT-CWT and region covariance based computational framework is successfully applied to classify the cancer cell line images. These feature parameters reflect the large morphological diversity of the images. Notice, however, that our software learns the specific covariances of these features from the training set, so the model for each image class is not rigid and therefore allows for larger variation in the image data, while maintaining its high effectivity. We adopt a covariance-based approach by exploiting pixel-level attributes to construct local region descriptors encoding covariances of several attributes inside a region of interest. Pixel attributes are extracted using directional difference scores and the 2D DT-CWT coefficients. Since background regions occur frequently in a cancer cell line image, we randomly sample subwindows from the foreground image regions after foreground-background segmentation and each microscopic image is represented by covariance matrices of certain number of subwindows sampled randomly from the whole image. Finally, an SVM classifier is trained to learn the class boundaries. Promising classification results are obtained by our experiments, which reveal the ability of the proposed features to characterize breast and liver carcinoma cell line textures.

It is experimentally demonstrated in this study that discrimination of 14 different classes of human cancer cell lines can be accomplished with high accuracy. We have developed a classification software utilizing the above-mentioned methods to be used by biologists. The software can be tested at *http://signal.ee.bilkent.edu.tr/cancerCellLineClassificationEngine.html*. The work presented in this chapter is published in [66, 67, 68].

Chapter 3

Detection of Centroblasts in Follicular Lymphoma Images Using Scale-Space Representation

This chapter deals with the problem of centroblast (CB) detection in follicular lymphoma (FL) images. FL is a cancer of the lymphatic system and it is one of the commonly encountered lymphoid malignancies in the western world. FL is a B-cell lymphoma that has a follicular center cell origin [15, 69]. FL patients may require highly variable treatments depending on the level of aggressiveness of the disease. Aggressive (fast-growing) FL should be exposed to early treatment using aggressive chemotherapy, whereas treatment may not be necessary for indolent (slow-growing) FL, in which case patients have higher chances of survival [15]. Therefore, accurate treatment of FL is of vital importance, which relies on accurate risk assessment of the disease. FL risk stratification is currently performed by histological examination of FL tissue samples, as recommended by World Health Organization (WHO) [13]. According to this grading method, pathologists manually count the average number of malignant cells called centroblasts (CB) in ten standard microscopic high-power fields (HPF) randomly selected from hematoxilin and eosin (H&E) stained FL tissue sections. FL grading is then performed based on the average CB count per HPF as follows: grade I (0-5 CB/HPF), grade

II (6-15 CB/HPF) and grade III (16 CB/HPF or higher).

Qualitative visual assessment of FL slides is a time-consuming and diligent task, and subject to substantial inter- and intra-reader variability [14]. Visual image interpretation by human readers also suffers from the sampling bias, which is caused by the random choice of ten HPFs in counting CB cells. The histological grading method tends to be biased, especially if the distribution of malignant cells exhibits high heterogeneity, thereby leading to inconsistent and unreliable clinical decisions that may misguide patient treatment. Computerized image analysis, on the other hand, allows for exploitation of quantitative features extracted from FL images and reduces the subjectivity in clinical decision-making process. Quantitative FL image analysis tools can potentially guide pathologists to review only relevant areas of the microscopic tissues or only slides with relevant information, which would alleviate the sampling bias. Computer-aided FL grading system is highly required in a clinical setting to help pathologists in this difficult task. A sample H&E-stained FL image is shown in Figure 3.1 and typical CB and non-CB cells are shown in Figure 3.2(a) and 3.2(b), respectively.

In this chapter, a new algorithm based on scale-space image representation is presented for computer-aided detection of CB cells in H&E stained FL tissue samples. Blob-like cellular structures in FL images are detected by deriving the scale-space extrema of the difference-of-Gaussians (DoG) pyramid as used in the well known Scale-Invariant Feature Transform (SIFT) algorithm. For classification of the detected cells, statistical region features, gray-level co-occurrence matrices (GLCM), gray-level run-length matrices (GLRLM) and SIFT descriptor are utilized and the resulting feature vectors are trained using a quadratic discriminant analysis (QDA) classifier. Elimination of false positives is achieved in a two-stage procedure where size information provided by the scale of the detected blobs is exploited in the first stage and the trained QDA model is used to further refine the detection process. The detection performance of the proposed system is compared with a direct application of the SIFT algorithm and with human readers.

The rest of the chapter is organized as follows. In Section 3.1, related work on

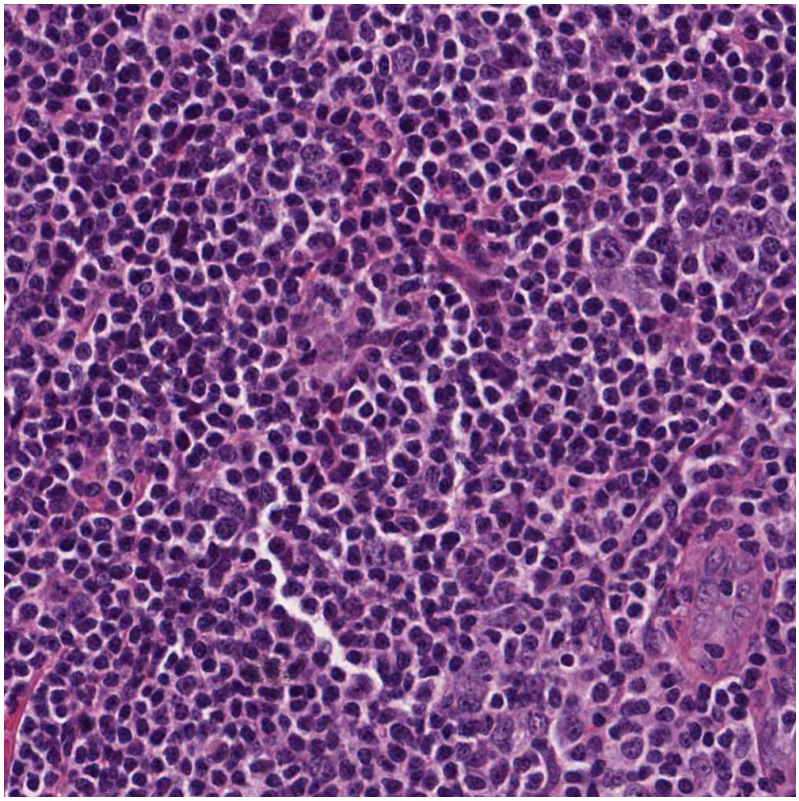

Figure 3.1: Sample image of H&E-stained FL tissue sections at 40x magnification.

computer-aided FL grading is presented. Section 3.2 describes the major steps of the CB detection procedure. Image binarization and DoG based blob-like cell detection algorithm is presented in Section 3.3. It is explained in Section 3.4 how classification of the detected cells is achieved. Finally, Section 3.5 presents the experimental results.

3.1 Related Work on Follicular Lymphoma Grading

Various computerized methods have been devised to carry out a quantitative analysis of FL images. Model-based intermediate representations (MBIR) are

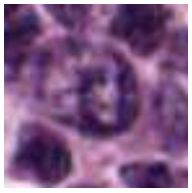

(a) CB

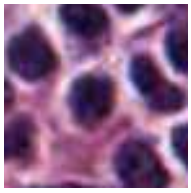

(b) non-CB

Figure 3.2: Sample images of a typical (a) centroblast cell and (b) non-centroblast cell.

employed to model the spatial distribution of cytological components in FL images and perform grading on an image level [15]. In MBIR, cytological regions are represented by ellipses and some geometric measures are introduced to describe the topological and morphological tissue characteristics. Some topological measurements include the number of neighboring nuclei and cytoplasm components for each nuclei, closest distance to a nuclei and a cytoplasm component for each nuclei, and average distance to neighboring cytoplasm components for each cytoplasm. Morphological features include major axis length, minor axis length and area of the ellipse, whose statistical parameters such as mean, standard deviation and skewness are used for analysis. These measurements summarize the FL image content and suffice to perform grading of FL images without counting CBs. Adaptive cellular likelihood based cell segmentation and gray-level run-length matrix (GLRLM) method is proposed to identify cellular regions and to differentiate CB cells from non-CB cells [16]. Locally adaptive thresholding strategy is used in combination with fast radial symmetry transform to separate clustered cells. In [17], local image patch descriptors are obtained by extracting the averaged local Fourier transform (LFT) features from a color space, called the most discriminant color (MDC) space, which is determined by iterative optimization of color space transformation and projection matrices with respect to Fisher-Rao discrimination criterion. Touching-cell splitting algorithm based on concave point detection and iterative cell-clump splitting is proposed to refine the segmentation obtained through MDC. [70] utilizes the Fourier spectrum of the cell regions combined with PCA to extract color texture features and classify CB and non-CB cells on cropped image regions. Mean shift algorithm combined with

hierarchical grouping is used in LUV color space for segmentation of individual cells [71]. Area, nuclear to cytoplasm ratio, mean and standard deviation of the intensity range within the cell are utilized as features for CB classification. In [72], follicles are detected in the first stage from immunohistochemically (IHC) stained microscopy images using the homogeneity feature of the co-occurrence matrix and then CB cells are identified in the resulting follicular regions.

3.2 The Detection Procedure

In this thesis, computerized detection of CB cells is accomplished by considering cellular regions as blob-like structures, which can be detected by scale-space image representation. Constituting an approximation to LoG method [73], DoG pyramid proposed in the SIFT algorithm [74, 19] is used for blob-like cellular region detection. Scale-space extrema points of the DoG pyramid yield the desired cell locations and sizes determined from the scale of detection. A simulated image with blobs of different sizes and a real FL image are shown in Figure 3.3 along with the detection results obtained by deriving the scale-space extrema of the DoG images.

There are several biomedical image analysis studies in the literature, that model the cell detection problem as a blob detection problem. In [75], multi-scale LoG filtering is performed to detect seed points for the subsequent initial segmentation of nuclear images based on local-maximum clustering. Fixed-scale LoG blob detector was used in [76] and [77] to detect and count nuclei in retinal images. This approach has the disadvantage of requiring the adjustment of the diameter of the LoG filter, which is impractical in situations where cells of varying sizes have to be handled, as is the case in FL. LoG filtering based automated cell detection algorithm in IHC stained tissues was presented in [78]. This method also needs to match the scale of the LoG filter to cell size and thus applies a number of LoG filters with different scales, leading to a computationally expensive process.

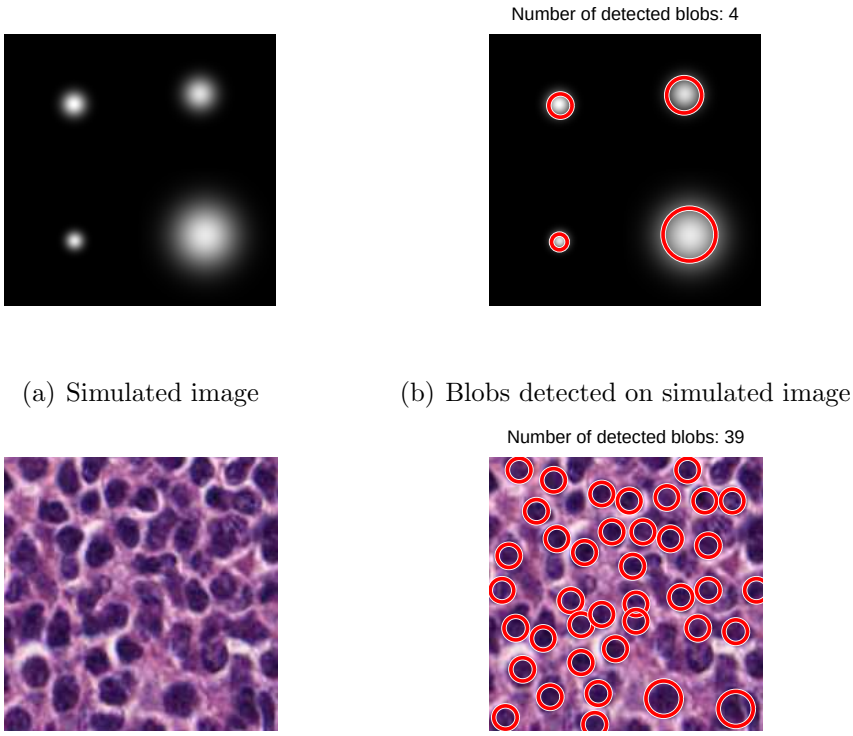

(a) Simulated image

(b) Blobs detected on simulated image

(c) FL image patch

(d) Blobs detected on FL image patch

Figure 3.3: Sample simulated (a) and real (c) images along with the detection results (b), (d) indicating the blob-like structures in the images by using red circles whose radius is determined from the scale at which the blob is detected

We propose a novel blob-like cell detection approach incorporating an effective image binarization step that boosts the performance of feature detection as applied in SIFT. Unlike [75] and [78] where LoG-based blob detection is carried out as a step that reinforces previous and/or subsequent steps for segmentation, we utilize DoG for scale-space blob detection from the binarized image without having to achieve the segmented cell boundaries. Unlike [76], [77] and [78] where fixed-scale LoG filters are employed for blob-like cell detection, our approach uses a multi-scale blob detector, allowing us to extract cells of various sizes from different levels of the DoG pyramid, which is computationally more efficient than applying different size LoG filters repeatedly. Identification of candidate CB regions using scale-space approach is followed by false positive reduction stages. Size information, which is an innate property of the scale-space processing, is

sufficient to eliminate most of the false positives. To refine the detection procedure, statistical and textural features are employed to further reduce the number of false positive cells, which is explained in Section 3.4. Major components of the proposed image analysis algorithm for CB detection are shown on Figure 3.4. In the training phase, CB and non-CB cells are manually cropped from the training set. Statistical and textural features are extracted from the cropped regions and the resulting feature vectors are trained using a QDA classifier. In the testing phase, multi-scale blob detection is carried out on the binarized FL images and the detected cells retained after size-based FP elimination are classified using the trained QDA model.

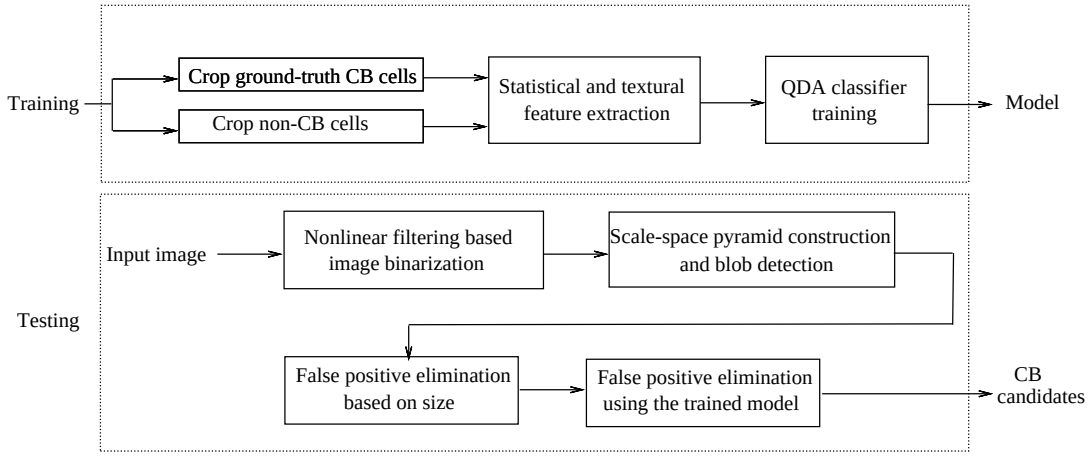

Figure 3.4: Image processing pipeline for the proposed CB detection system.

3.3 Centroblast Detection via Scale-Space Approach

In this section, the steps of the proposed centroblast detection algorithm utilizing DoG based scale-space image representation are described in detail.

FL images are composed mostly of small cleaved cells called centrocytes and larger non-cleaved cells called centroblasts in addition to extracellular material. Due to the characteristics of the H&E staining, CB and non-CB cells appear

to be dark blob-like regions in each channel of the RGB FL image. We aim to detect those dark structures in a relatively lighter colored surroundings by using the scale-space extrema of the difference-of-Gaussian (DoG) images as in [74]. DoG, however, fails to reveal the cellular image structures in FL as CB cells often exhibit heterogeneous tissue characteristics, resulting in poor CB detection performance. In order for the Gaussian blob detector to function properly, the input image structures should be distinguishable from the background so that desired cells will not be missed. We propose an image binarization step to allow for an easier identification of cellular regions. In Section 3.3.1, we demonstrate how FL image binarization using nonlinear filtering contributes to the accuracy of cell detection and in Section 3.3.2 we explain the procedure for constructing scale-space pyramids and detecting blob-like cell structures.

3.3.1 Nonlinear Filtering Based FL Image Binarization

The performance of cell detection procedure may be degraded by spatial tissue characteristics of centroblast regions comprising more nucleoli components than non-centroblast regions, thereby making them less differential with respect to background. Hence, it is possible to miss some CB cells in the detection phase if the scale-space pyramid is built from the original image without taking into account the specific cell properties. An image binarization methodology is applied to capture the highest number of cellular regions in FL images.

Standard deviation filtering is performed on the gray-level image $I(x, y)$ by computing the standard deviation of a square region around each pixel. $I(x, y)$ is divided by the resulting image $S(x, y)$ to obtain the image

$$J(x, y) = \frac{I(x, y)}{S(x, y)} \tag{3.1}$$

where flat regions are amplified and intensity values are normalized with respect to local variance. Then, the image

$$H(x, y) = I(x, y) + cJ(x, y) \tag{3.2}$$

where c is a constant multiplier chosen as $c = 3$, is likely to have foreground and

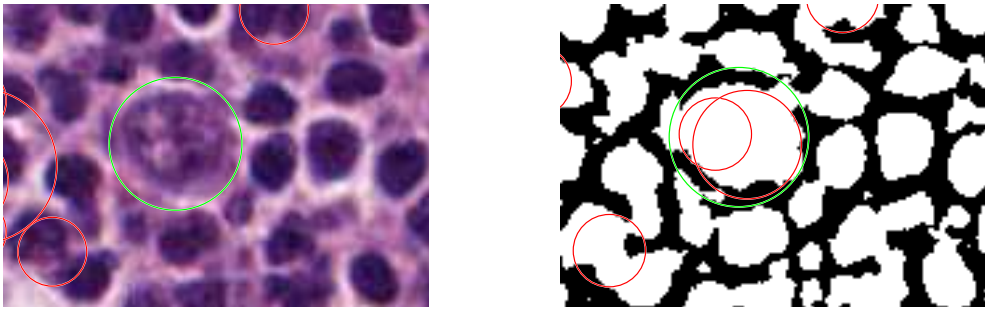

(a) Original image (b) Binarized image

Figure 3.5: Detection results for a sample image patch showing (a) the original version and (b) the binarized version

background that can be readily discriminated, as compared to the original image $I(x, y)$ since the nonlinear filtering and normalization operations performed above help emphasize the distinction between cellular regions and the background. We subtract the Gaussian smoothed version $H_l(x, y)$ of $H(x, y)$ from itself to obtain a high-frequency image

$$H_h(x, y) = H(x, y) - H_l(x, y) \tag{3.3}$$

on which Otsu thresholding [56] is performed. Morphological opening is applied to the resulting binary image to obtain the input image from which scale-space pyramid is constructed.

Hispathological tissue specimens belonging to FL possess certain characteristics that make it difficult to capture the targeted CB cells. An important difference between CB and non-CB cells is that CB has a rough and irregular texture as opposed to almost homogeneous texture observed in non-CBs. It is therefore necessary to devise an algorithm that forces CB cells to stand out from their surroundings. The abovementioned binarization algorithm accomplishes this by performing standard deviation filtering, normalization and thresholding operations, taking into account the CB cell morphology. Detection results on both the original and the binarized versions of a small image patch are shown in Figure 3.5. In this figure, green circles represent ground-truth CB locations marked by at least three out of six pathologists and red circles indicate locations detected by scale-space representation with radius showing the scale at which the blob

is detected. CB cell in Figure 3.5(a) has an irregular texture and can not be identified by direct application of DoG method. In binarized image in Figure 3.5(b), it can be easily distinguished from the background and detected using DoG method. Large blobs falsely identified in Figure 3.5(a) due to merging of several blobs in coarser scales of the pyramid are eliminated in the binary image 3.5(b). The proposed binarization approach provides a noticeable distinction between cellular regions and background, which is lacking in the original image due to morphological properties of CB cells. Figure 3.6 depicts the detection results for both the original image and the binarized image of a larger region. As can be seen from the results, two CB cells missed in detection from the original image can be distinguished if CB detection is carried out on the binarized image. These examples demonstrate that standard deviation filtering based image binarization may boost the performance of the CB detection process.

3.3.2 Detection of Cells Using Scale-Space Image Representation

Proper localization of CB cells in FL largely depends on the capability of the detection method to identify candidate regions with high accuracy. The first step in CB/non-CB classification is the detection of candidate CB regions that will then be subject to statistical and textural analysis for discrimination of CBs from non-CBs. In [16], Sertel *et al.* employ the expectation maximization (EM) algorithm to fit a Gaussian mixture model to the distribution of cellular and extracellular components. Using the posterior probability of each pixel belonging to cellular components, a cellular-likelihood image is generated on which adaptive thresholding is performed to obtain the binary image consisting of candidate cell regions.

In this study, we bypass the step of precise segmentation of candidate cellular structures by attempting to detect the centers of cells without the need to determine the exact cell boundaries. To this end, we propose to take advantage of the scale-space theory, specifically, the linear scale-space representation [79], for

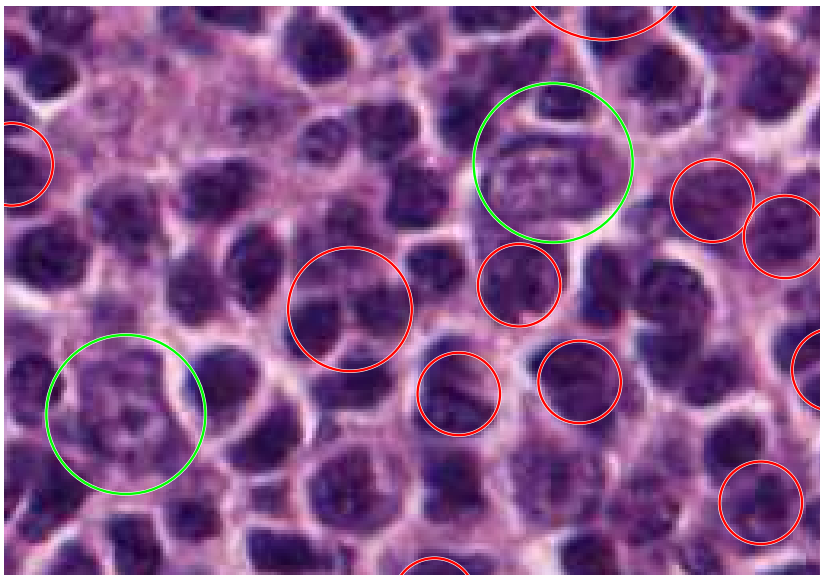

(a) Detection results using the original image

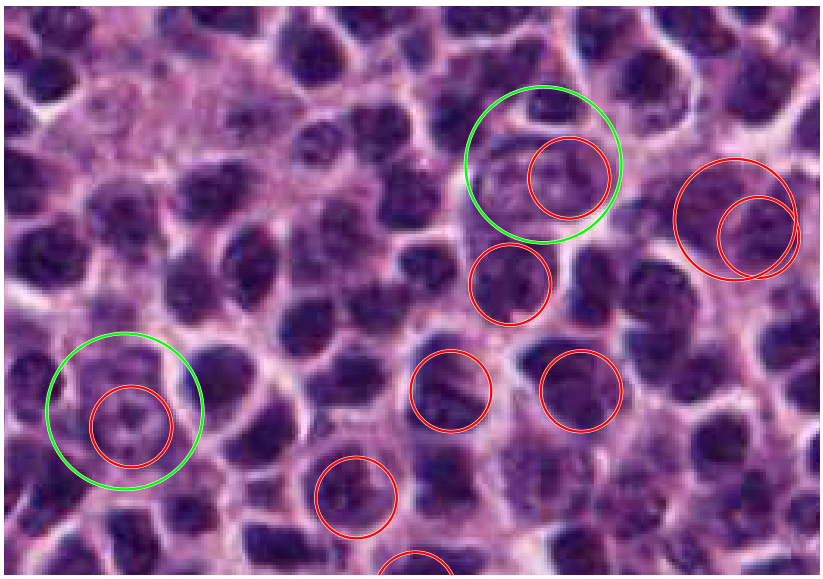

(b) Detection results using the binarized image

Figure 3.6: Cellular region detection results for a sample image patch using (a) the original image and (b) the binarized image

identification of salient locations that are likely to correspond to cellular regions. Scale-space theory provides a convenient framework for analysis and derivation of image components, objects, etc. from different scales. Scale-space of an image can be obtained by convolving the image with a scale-space kernel parametrized by the scale variable [80]. Lindeberg [73], Koenderink [80] and Babaud *et. al.* [81] has proved that the Gaussian kernel is the only scale-space kernel that satisfies the conditions as stated by scale-space axioms, such as linearity, shift invariance, semi-group structure and non-creation of local extrema. Formally, linear scale-space representation $L(x, y; \sigma)$ of a given image $I(x, y)$ is given by the solution to the heat diffusion equation [18]

$$\partial_\sigma L = \sigma \nabla^2 L \tag{3.4}$$

where the initial condition is $L(x, y; 0) = I(x, y)$. The solution is found to be the convolution of a rotation-invariant Gaussian function $G(x, y; \sigma)$ parametrized by the scale with the image $I(x, y)$:

$$L(x, y; \sigma) = G(x, y; \sigma) * I(x, y) \tag{3.5}$$

where the Gaussian kernel is given by

$$G(x, y; \sigma) = \frac{1}{2\pi\sigma^2} e^{-\frac{(x^2+y^2)}{2\sigma^2}} \tag{3.6}$$

It has been demonstrated in [18] that scale-space extrema of the scale-normalized Laplacian of Gaussian $\sigma^2 \nabla^2 L$ correspond to blob-like structures in the image, which can be defined as regions appearing darker or brighter than the background [82]. In the well-known Scale-Invariant Feature Transform (SIFT) algorithm, Lowe [19] has proposed to use the difference-of-Gaussian function as an approximation to the scale-normalized Laplacian of Gaussian for the purpose of detecting salient locations in the image, namely, the keypoints.

Localization of candidate cell regions in FL images is accomplished by building the scale-space pyramid as in [74]. The input image is first interpolated by a factor of 2 before pyramid construction to retain high-frequency details, thereby restricting the frequency spectrum of the image to $[0, \pi/2]$ range. This would prevent the loss of fine details in successive smoothing and downsampling operations performed at each level of the pyramid. Let $I_i(x, y)$ denote the input image

at the i^{th} level of the pyramid. $I_i(x, y)$ is smoothed using the Gaussian kernel to obtain the smoothed image $L_{s_i}(x, y)$:

$$L_{s_i}(x, y; \sigma) = G(x, y; \sigma) * I_i(x, y) \tag{3.7}$$

$L_{s_i}(x, y)$ is smoothed using the Gaussian kernel with the same σ to obtain the image $L_{g_i}(x, y)$:

$$L_{g_i}(x, y; \sigma) = G(x, y; \sigma) * L_{s_i}(x, y; \sigma) \tag{3.8}$$

The effective smoothing factor of $L_{g_i}(x, y)$ is $\sigma\sqrt{2}$. The difference-of-Gaussian image is obtained by computing the difference of the Gaussian smoothed images:

$$\begin{aligned} D_i(x, y; \sigma) &= L_{g_i}(x, y; \sigma) - L_{s_i}(x, y; \sigma) \\ &= (G(x, y; \sigma\sqrt{2}) - G(x, y; \sigma)) * I_i(x, y) \end{aligned}$$

where the ratio between the Gaussian kernels is $\sqrt{2}$. The scale parameter is selected to be $\sigma = \sqrt{2}$ as in [74]. For the next level of the pyramid, $L_{g_i}(x, y)$ is subsampled by a factor of 1.5 using bilinear interpolation to obtain the image $I_{i+1}(x, y)$ that would be input to the next pyramid level.

Performing the above operations, we construct the difference-of-Gaussians pyramid $\{D_i(x, y; \sigma)\}_{i=1}^{N}$, which constitutes a scale-space representation of the input image using N levels. Scale-space extrema of the scale-space function $\{D_i(x, y; \sigma)\}_{i=1}^{N}$ yield the desired blob-like image structures, which, in case of FL, correspond to centroblast and non-centroblast regions. Since scale-space minima (maxima) reveal dark (bright) blobs in a bright (dark) environment [82], we search for local minima points in scale-space as the green channel of the RGB image is used as the intensity image. For each pixel, scale-space minima of $\{D_i(x, y; \sigma)\}_{i=1}^{N}$ are derived by first comparing the center pixel to its 8 neighbors at the same pyramid level [74]. If it is a minimum at this scale, we proceed to the lower level to find the corresponding point and compare the target pixel to 9 neighbors including the corresponding point and its 8 neighbors. If the target pixel is still a minimum, the same procedure is applied for the upper level. Scale-space extrema locations thus found are acknowledged as candidate CB regions for further processing.

3.4 Cell Classification

Cellular region detection via scale-space approach provides candidate locations for CB cells. Each detected cell is associated with a certain location and scale determined by the spatial position and scale of the scale-space extremum point. A scale-space extremum detected at $D_{\tilde{i}}(\tilde{x}, \tilde{y}; \sigma)$, $1 \leq \tilde{i} \leq N$, defines a blob with radius

$$r_{\tilde{i}}(\tilde{x}, \tilde{y}) = \frac{(\sigma\sqrt{2} + \sigma)}{2}(1.5)^{\tilde{i}-1} \tag{3.9}$$

by taking the average of the consecutive scales $L_{g_{\tilde{i}}}(x, y; \sigma)$ and $L_{s_{\tilde{i}}}(x, y; \sigma)$ between which the blob is detected, and with spatial position

$$(\frac{(1.5)^{\tilde{i}-1}}{2}\tilde{x}, \frac{(1.5)^{\tilde{i}-1}}{2}\tilde{y}) \tag{3.10}$$

The inner cell texture and scale-space size information may constitute significant prognostic clues facilitating the discrimination of CBs from non-CBs among the detected cells. Size information and textural and statistical region properties are utilized in a two-stage false positive elimination procedure to classify CB and non-CB cells.

3.4.1 FP Elimination Using Size Information

In the first stage, we refine our estimates of CB cells based on the *a-priori* knowledge about the CB cell sizes. The radius of the cellular structures in FL images is, in general, between the range 6 and 30. Thus, after scale-space extrema selection, only those blobs whose radius is in the range $[6, 30]$ are taken into consideration as possible CB cells. One of the most essential differences between CB and non-CB cells is that CBs are generally larger than non-CBs. We aim to reduce the false positive rate by restricting the acceptable range to $[10, 30]$. Hence, the first stage false positive elimination is performed as

$$\mathrm{C}_{\tilde{\mathrm{i}}}(\tilde{\mathrm{x}}, \tilde{\mathrm{y}}) = \begin{cases} \mathrm{CB}, & \text{if } r_{\tilde{i}}(\tilde{x}, \tilde{y}) \in [10, 30] \\ \mathrm{nonCB}, & \text{otherwise} \end{cases}$$

where $C_{\tilde{i}}(\tilde{x}, \tilde{y})$ is the scale-space blob detected at $D_{\tilde{i}}(\tilde{x}, \tilde{y}; \sigma)$. We employ the radius information conveyed inherently by scale-space processing to alleviate the number of false positive cells.

3.4.2 Statistical Features

In the second stage, statistical region features, such as mean, variance, entropy, skewness and kurtosis, along with the gray-level co-occurrence matrix (GLCM) and gray-level run-length matrix (GLRLM) properties are computed to form a feature vector that encodes the spatial arrangement of cellular regions in a statistical and textural framework. Skewness and kurtosis have been shown to constitute distinctive features in detection of microcalcifications in mammogram images [83]. Second and third order statistics were utilized in biomedical signal processing to characterize the sleep spindles occurring in electroencephalogram (EEG) records of human sleep [84]. All these features are extracted from a circular region R around each detected point. Let $p(x)$ denote the probability density function of the intensities in R. The pdf $p(x)$ is estimated from pixel values and used in discrete form. For each detected cell that is not eliminated in the first stage, we estimate the following statistical parameters:

$$\mu = \int_{x \in R} x p(x)\, dx, \tag{3.11}$$

$$\sigma^2 = \int_{x \in R} (x - \mu) p(x)\, dx, \tag{3.12}$$

$$h = \int_{x \in R} -p(x) \log p(x)\, dx, \tag{3.13}$$

$$\gamma_1 = \int_{x \in R} (\frac{x - \mu}{\sigma})^3 p(x)\, dx, \tag{3.14}$$

and

$$\gamma_2 = \int_{x \in R} (\frac{x - \mu}{\sigma})^4 p(x)\, dx \tag{3.15}$$

where μ, σ^2, h, γ_1 and γ_2 denotes the mean, variance, entropy, skewness and the kurtosis, respectively.

3.4.3 Textural Features

GLCM is a 2-D matrix representation of image texture proposed by Haralick *et al.* [85]. It is a 2-D histogram of neighboring image pixels in one of the four directions $\{0, \pi/4, \pi/2, 3\pi/4\}$. Each entry $p(i, j)$ of a co-occurrence matrix is computed as the number of times the gray-levels i and j are neighbors in a specific direction. Four different GLCMs of an 8-level quantized region are computed for four directions, and four properties, namely, contrast, correlation, energy and homogeneity, are extracted from each 8-by-8 GLCM. These features are averaged over four directions and we obtain four GLCM features for each detected region.

Proposed by Galloway [86], GLRLM characterizes the texture of a region by computing the gray-level runs and constructing a 2-D matrix representation. Each entry $p(i, j)$ of a run-length matrix can be obtained as the number of runs of gray-level i in a specific direction with run length j. We compute four different GLRLMs of an 8-level quantized cellular region for four different angles $\{0, \pi/4, \pi/2, 3\pi/4\}$ and derive eleven run-length features averaged over these angles, which are, namely, short-run emphasis, long-run emphasis, gray-level nonuniformity, run-length nonuniformity, run percentage, low gray-level run emphasis, high gray-level run emphasis, short-run low gray-level emphasis, short-run high gray-level emphasis, long-run low gray-level emphasis and long-run high gray-level emphasis.

3.4.4 SIFT Descriptor

SIFT descriptor [19] is also utilized in the second stage as an alternative to statistical and textural features in false positive elimination. As blob-like cellular structures are detected using a modified version of the feature detection part of the SIFT algorithm, we can compute SIFT descriptors on detected scale-space extrema locations, namely, the keypoints in SIFT terminology.

Each keypoint is first assigned an orientation computed from the local image

neighborhood. This would provide rotation invariance by subtracting the orientation from the descriptor representation. For each detected point, the Gaussian smoothed image $L_{s_i}(x, y; \sigma)$ at a certain scale i that corresponds to average cell size in FL is used to calculate the gradient magnitude and orientation images, respectively:

$$m(x, y) = \sqrt{a^2 + b^2}, \tag{3.16}$$

and

$$\theta(x, y) = \arctan(\frac{b}{a}) \tag{3.17}$$

where

$$a = (L_{s_i}(x + 1, y) - L_{s_i}(x - 1, y)), \tag{3.18}$$

and

$$b = (L_{s_i}(x, y + 1) - L_{s_i}(x, y - 1)) \tag{3.19}$$

We construct an orientation histogram weighted by gradient magnitudes of each sample, using the gradient orientations of local neighborhood around the detected point. Peak detection is performed on the orientation histogram to obtain the local image orientation.

In the descriptor computation part, 8-bin orientation histograms are created in each of the 16 4-by-4 subregions contained in 16-by-16 region of $L_{s_i}(x, y; \sigma)$ around the keypoint. Each sample is again weighted by its gradient magnitude. SIFT keypoint descriptor is obtained as the collection of 16 8-bin orientation histograms representing the image content over 4-by-4 subregions in the neighborhood of the keypoint. Hence, it is a 128 element feature vector for each detected blob. VLFeat library [87] is used for SIFT implementation.

3.4.5 Classifier Learning

As shown in Figure 3.4, positive (CB) and negative (non-CB) samples are manually cropped from the training images in the training phase to generate a classification model. Statistical features and GLCM, GLRLM and SIFT properties are calculated in cropped cell regions. CB cells are cropped from ground-truth locations that are marked by at least two out of six pathologists and non-CB cells

are selected among those cells that are not marked by any of the pathologists. A scatter plot of the 20 features containing statistical, GLCM and GRLRM features in 2D principal component analysis (PCA)-reduced space is shown in Figure 3.7, where the two dimensions correspond to the two eigenvectors with the largest eigenvalues. Figure 3.8 depicts the same plot for SIFT features. Quadratic discriminant analysis (QDA) classifier is used to learn the decision boundary between CB and non-CB cells. In the testing phase, feature vectors extracted from the detected cells retained after the 1^{st} refinement stage are fed to the learned model to obtain the classification labels. Both CB and non-CB cells of the training set are modeled as Gaussian distributions with arbitrary covariance matrices, and Bayesian classification is performed. The cost matrix of this QDA classifier is parametrized by the cost of assigning a non-CB sample to CB as

$$Cost(p) = \begin{bmatrix} 0 & p \\ 1 & 0 \end{bmatrix} \tag{3.20}$$

where the parameter p determines the decision boundary and balances the tradeoff between sensitivity and number of false positives.

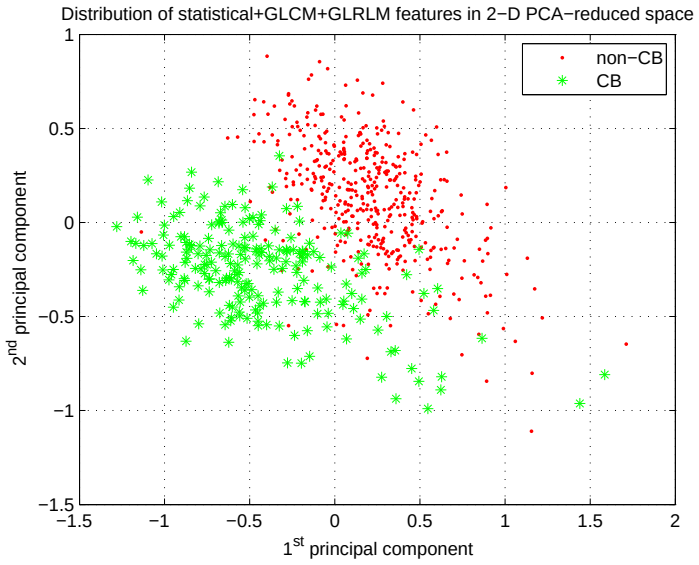

Figure 3.7: Scatter plot of statistical and textural (GLCM and GLRLM) features extracted from cropped cells of training images

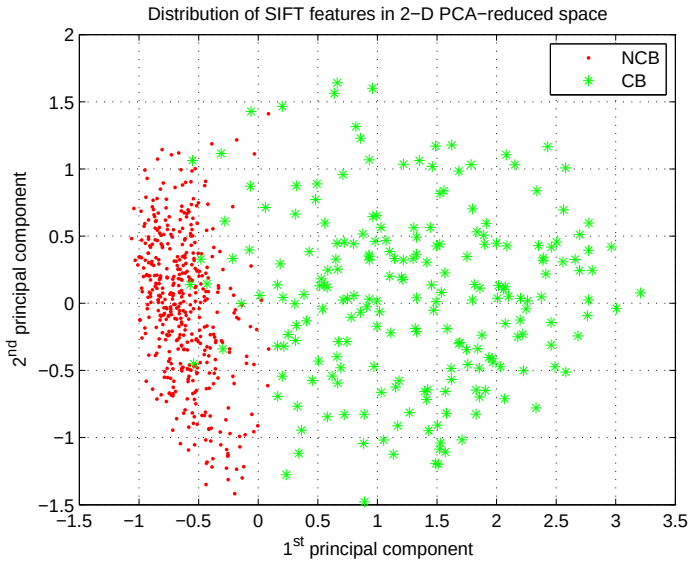

Figure 3.8: Scatter plot of SIFT features extracted from cropped cells of training images

3.5 Experimental Results

The proposed CB detection algorithm is evaluated on a dataset of 30 H&E stained high-power field images of FL which shows a heteregenous character. Each image has size 1353x2168 and is digitized at 40x magnification by an Aperio Scope XT Scanner (Aperio, San Diego, CA). Six expert board-certified hematopathologists have created the ground-truth by individually marking the CB cell locations. Therefore, the proposed algorithm is evaluated against six different ground-truths, each consisting of cells identified by at least n out of six pathologists where n is ranging from one to six.

The first 15 images are used as training images and the remaining ones as test images. Ground-truth CB cells from the training images are cropped from locations marked by at least n pathologists. Non-CB cells are manually selected from cell locations where no pathologist identifies a CB. In the training phase, statistical, GLCM, GLRLM and SIFT features are computed in a circular region of radius 12 pixels around the center point for both CB and non-CB cells. In the testing phase, we compute these features in a circular region of radius 12 pixels

around the detected scale-space extremum point.

We first evaluate how exploitation of the size information of the detected scale-space blobs improves the CB detection procedure. In Section 3.4, range of radius values valid for cells in FL images is changed from $[6, 30]$ to $[10, 30]$ to get rid of small non-CB cells in the 1^{st} false positive elimination stage. Results of this stage are shown in Table 3.1, in which $Npath$ denotes the number of pathologists required to verify a cell, CB denotes the number of CB cells detected by our algorithm divided by the total number of CB cells, Sensitivity denotes the percentage of the detected CB cells among all CB cells, FP denotes the number of false positives and, normal range and restricted range correspond to $[6, 30]$ and $[10, 30]$, respectively. The findings presented here are averaged over 15 test images. These results demonstrate that multi-scale blob detection based on DoG provides valuable information that helps to reduce the number of false positives by almost 88% without compromising the sensitivity of the system much. For instance, if we require the consensus of at least four pathologists to verify a CB cell, sensitivity is reduced by 2.3% while the number of false positives decreases by 87.6%.

Table 3.1: Results of the 1^{st} FP Elimination Stage

	normal range			restricted range		
Npath	CB	Sensitivity (%)	FP	CB	Sensitivity (%)	FP
1	306/337	90.8	3642	174/337	51.6	448
2	139/148	93.9	3653	129/148	87.2	451
3	78/82	95.1	3657	75/82	91.5	455
4	43/43	100	3660	42/43	97.7	457
5	17/17	100	3661	16/17	94.1	459
6	1/1	100	3663	1/1	100	460

We also investigate the effect of the proposed image binarization strategy on the detection results. Table 3.2 shows the results of the 1^{st} FP elimination stage without using image binarization. Comparative analysis of Tables 3.1 and

3.2 leads to the observation that the sensitivity of the system without applying binarization is far below that when binarization is applied before DoG based blob-like cell detection. In case of the consensus of at least four pathologists, for instance, the sensitivity without binarization in the restricted range is 67.4% whereas it is 97.7% if binarization is performed, with almost the same number of FPs.

Table 3.2: Results of the 1^{st} FP Elimination Stage Without Binarization

	normal range			restricted range		
Npath	CB	Sensitivity (%)	FP	CB	Sensitivity (%)	FP
1	306/337	90.8	3257	158/337	46.9	442
2	140/148	94.6	3268	106/148	71.6	446
3	77/82	93.9	3272	62/82	75.6	449
4	40/43	93	3275	29/43	67.4	451
5	15/17	88.2	3277	10/17	58.8	452
6	1/1	100	3278	0/1	0	453

Secondly, the effect of the 2^{nd} FP elimination stage on sensitivity and the number of FPs is explored. We compare the performance of five different sets of feature vectors as described in Table 3.3. The first four feature vectors are used in a scenario where DoG based scale-space blob detection is performed on binarized images as described in this paper. The last feature vector, which we denote by direct SIFT, is again the SIFT descriptor, but used in a scenario where blob detection is performed on original images, which is basically a direct application of SIFT.

Figures 3.9-3.11 show the ROC curves plotted for the sensitivity versus the number of false positives in test set as the parameter in Equation (3.20) is changing, evaluated with respect to six different ground-truths. The findings presented on these plots are averaged over 15 test images. Ten different p values are used to plot the curves, but the range of these values differs among five feature vectors. Examining the ROC curves generated from training images in each of the

Table 3.3: Feature Sets Used in Cell Classification

Feature Sets	Features	Number of features
Feature Set 1 (FS1)	Statistical and GLCM	9
Feature Set 2 (FS2)	Statistical and GLRLM	16
Feature Set 3 (FS3)	Statistical and GLCM and GLRLM	20
Feature Set 4 (FS4)	SIFT	128
Feature Set 5 (FS5)	Direct SIFT	128

five cases, we attemp to determine a range for p that yields reasonable trends in sensitivity-FP trade-off. Once an acceptable range for p is found, we identify the optimum decision point, which corresponds to one of the values assumed by p, in sensitivity-FP plot from the training set. As a general rule, it is enforced that at least 40 FPs must be eliminated in return for a 1% decline in sensitivity. These optimum points are indicated by green circles in Figures 3.9-3.11.

As can be seen from the results, Feature Set 1 (FS1) outperforms all other feature vectors in all of the six cases. Using statistical and GLCM features, it is possible to attain 97% sensitivity with approximately 230 FPs for $Npath = 4$, and 91% sensitivity with approximately 210 FPs for $Npath = 3$. It is observed that all three feature vectors that we have proposed (FS1, FS2 and FS3) are clearly superior to the SIFT descriptor, which could not reduce the number of FPs down below 350 in any of the six cases. Furthermore, direct application of SIFT descriptor, direct SIFT, leads to poor detection performance, with 75% sensitivity versus 450 FPs for $Npath = 3$ as the best result. This proves that FL image binarization applied prior to scale-space blob detection is of crucial importance in CB detection. Our system is capable of detecting approximately 90% of the CB cells with an approximate FP rate of $200/3000 \approx 7\%$, substantially reducing the search space of pathologists.

SIFT descriptor is particularly well suited for computer vision tasks such as object detection [19], but it may not be as effective in the field of microscopic image analysis. Experimental results suggest that combination of GLCM and

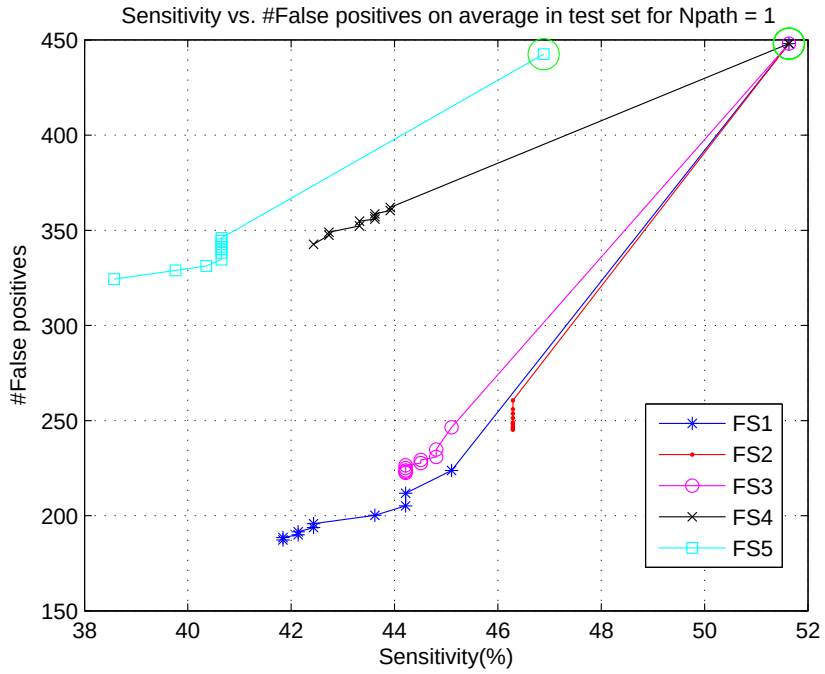

(a) ROC curve for $Npath = 1$

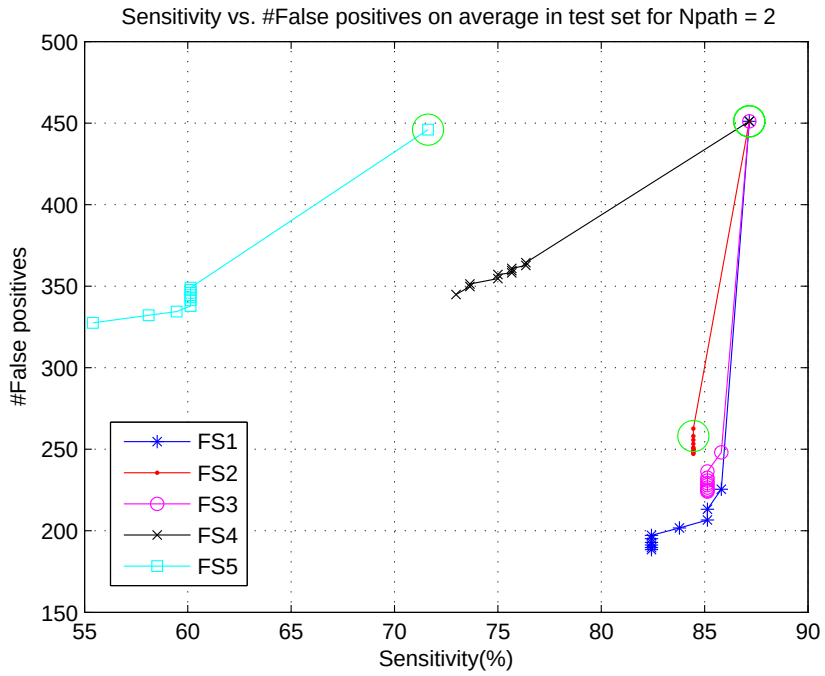

(b) ROC curve for $Npath = 2$

Figure 3.9: ROC curve of average sensitivity (%) versus average number of false positives in the test set for (a) $Npath = 1$ and (b) $Npath = 2$

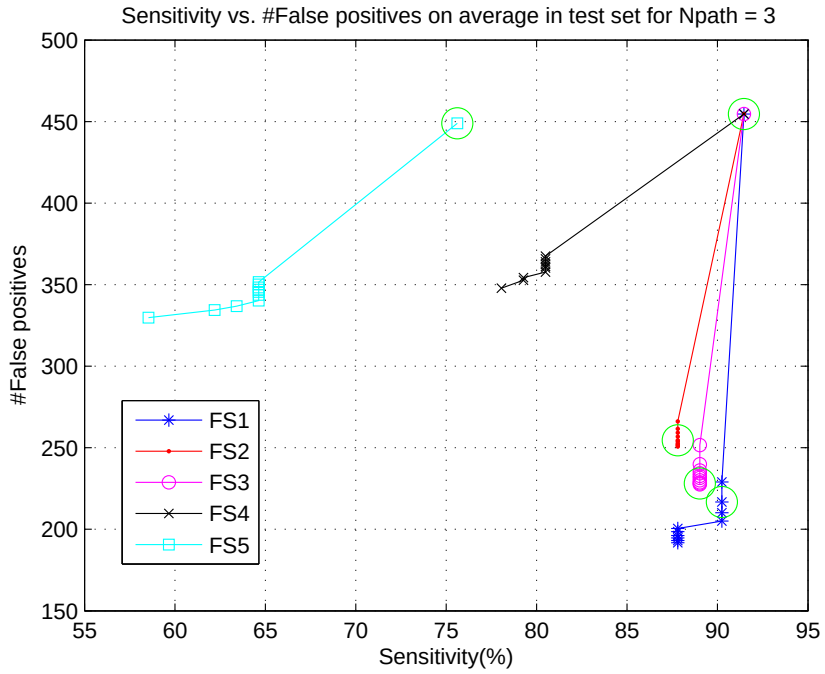

(a) ROC curve for $Npath = 3$

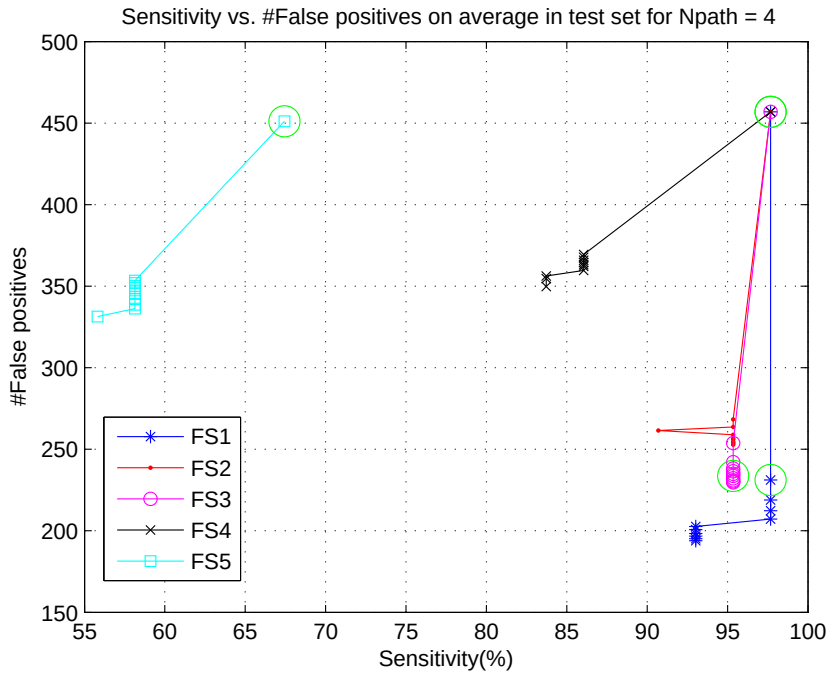

(b) ROC curve for $Npath = 4$

Figure 3.10: ROC curve of average sensitivity (%) versus average number of false positives in the test set for (a) $Npath = 3$ and (b) $Npath = 4$

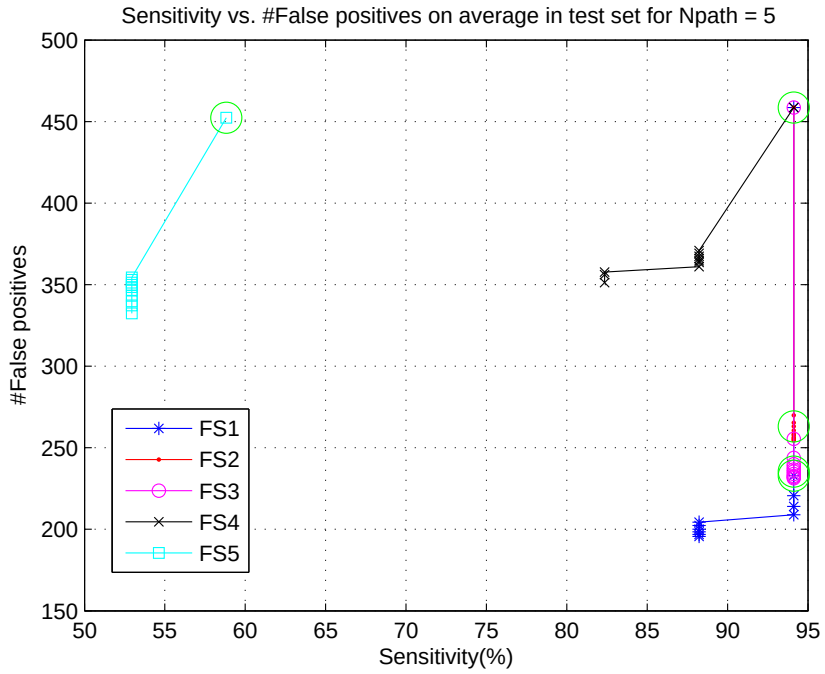

(a) ROC curve for $Npath = 5$

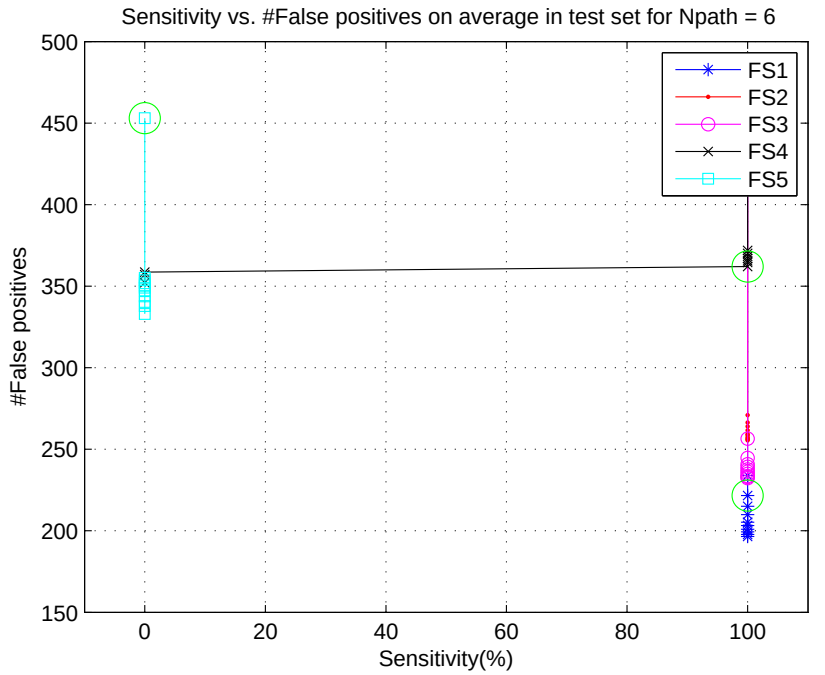

(b) ROC curve for $Npath = 6$

Figure 3.11: ROC curve of average sensitivity (%) versus average number of false positives in the test set for (a) $Npath = 5$ and (b) $Npath = 6$

statistical features leads to a more robust detection performance as compared to SIFT. GLCM and GLRLM are both convenient for texture analysis and classification, whereas SIFT, which relies on gradient orientation histograms, tends to be more descriptive for real-world objects and scenes. Since cellular regions in FL images can be regarded as texture, the performance of SIFT is lower than GLCM and GLRLM based features in local cellular region representation, which is also confirmed by our experiments. Moreover, 128-length SIFT feature vector is much more computationally expensive in both feature computation and classification stages than the proposed feature sets. Utilizing keypoint detection part of SIFT in candidate cell detection and FS1 for elimination of FPs in cell classification yields the best detection results.

Finally, we assess the accuracy of human readers, the pathologists who have marked the dataset. Similar to the performance evaluation of the computer-aided detection algorithm, the performance of pathologists is evaluated against six ground-truths created by pathologists themselves. Table 3.4 presents the average sensitivity and the average number of FPs of six pathologists evaluated in six different cases depending on the minimum number of pathologists required to verify a CB cell. The results presented in Table 3.4 are averaged over 30 images in the dataset and then averaged over pathologists. It can be observed that the proposed computerized CB detection system, which achieves 97% sensitivity for $Npath = 4$, outperforms the accuracy of human readers, which is 75% based on the same ground-truth. However, the number of FPs generated by the algorithm (200-250) is higher than those generated by human readers (5-6).

Table 3.4: Accuracy of Human Readers

Npath	1	2	3	4	5	6
Average Sensitivity (%)	26.2	52.7	65.5	75.6	85.4	95.8
Average FP	1.9	2.2	3.8	5.3	6.8	8.2

3.6 Summary

A novel computerized cell detection algorithm is presented for accurate identification of malignant CB cells in FL images. The proposed algorithm utilizes the scale-space representation of FL images to detect blob-like cellular structures. Directly applying the scale-space DoG pyramid of SIFT to original FL images results in unsatisfactory CB detection performance due to the specific textural characteristics of CB regions. We introduce an image binarization strategy that successfully surmounts this problem by achieving the differentiation of CBs from surroundings in the binarized image. False positive reduction strategies incorporate size constraints and statistical and textural features on candidate CB regions. Experimental results indicate that the accuracy of our computer-aided CB detection system is higher than the SIFT algorithm. Furthermore, the proposed system outperforms the accuracy of human readers, thereby signaling the need for the development of quantitative analysis tools for histopathology imagery.

Chapter 4

Conclusions

In this thesis, new image processing methods are proposed for two different microscopic image analysis problems. The first problem concerns the classification of human cancer cell line images. Cancer cell lines are derived from cancerous regions of the human body and utilized in cancer research and drug discovery studies. Researchers need to deal with a large number of specimens in laboratory experiments and verify the identity of cell lines frequently. Classical methods developed for cell line authentication are costly and time-consuming, and an expert is required to carry out the biochemical tests. A computational framework employing image processing and machine learning techniques is developed for automated classification of cancer cell line images. In the second part of the thesis, the problem of centroblast detection in follicular lymphoma images is investigated. FL is a lymphoid malignancy commonly encountered in the western world and grading of FL is performed by pathologists who count the large malignant centroblast cells and stratify the FL case into three different grades based on the average number of centroblast in microscopic high-power fields. This method is subject to significant inter- and intra-reader variability and sampling bias. A new computerized method is proposed to detect centroblasts, which would facilitate the FL grading process.

Discrimination of cancer cell line images consisting of 14 classes is achieved by using the DT-CWT coefficients combined with the region covariance framework.

2D DT-CWT decomposition is applied to cell line images and magnitudes of coefficients at directional detail subbands are calculated and used as pixel features in covariance representation. A new feature called directional difference scores is proposed and included in covariance descriptor computations. Random subwindows are sampled from the whole image and covariance matrices are computed for each local window containing foreground cellular regions. It is experimentally observed that covariance features provide distinctive image representation for cancer cell line dataset, especially when combined with DT-CWT and directional difference score features. Orientation selectivity property of DT-CWT is shown to enhance the recognition rate in a considerable manner, thereby outperforming the conventional method of covariance feature extraction using only intensity and derivative features. Classification of extracted features are performed in the feature space obtained by vectorizing the covariance matrices, which are symmetric positive-definite, and SVM classifier is employed to determine the class boundaries. In addition, normalized version of covariance descriptors are tested on the same dataset and found to be more successful than classical covariance descriptors. Eliminating the disadvantages of conventional cell line verification methods, the proposed computerized system can be reliably utilized in laboratory studies. Our tool provides an automated, time- and cost-efficient analysis of cancer cell morphology to classify different cancer cell lines using image processing techniques, which can be used as an alternative to the costly short tandem repeat (STR) analysis.

A new computer-assisted method based on scale-space image representation is developed for FL grading. Detection of candidate centroblast cells is achieved based on the observation that cellular regions in FL images appear as dark blob-like structures in a relatively brighter environment. Scale-space blob detection method as applied in the SIFT algorithm uses the scale-space extrema of the difference-of-Gaussians pyramid constructed from successive convolutions of the input image with a Gaussian kernel. Direct application of this method fails over FL images due to the textural characteristics of centroblast regions, which require a more sophisticated approach. An image binarization strategy is proposed

and applied on FL images prior to scale-space blob detection algorithm, and experimentally shown to be effective in making centroblast regions more salient, thus improving the sensitivity of the detection system. To refine the detection procedure, statistical and textural analysis is carried out on the detected cells. Statistical features including mean, variance, entropy, skewness and kurtosis, two texture descriptors, namely, gray-level co-occurrence matrix and gray-level run-length matrix, and SIFT descriptor are employed to represent cellular regions in the feature space. Experimental results suggest that combination of statistical and textural features is quite successful in centroblast detection and outperforms the SIFT descriptor. These features have also smaller length and therefore lower computational complexity as compared to SIFT. Furthermore, experiments for evaluating the performance of pathologists marking the dataset demonstrate that the proposed algorithm provides better results than expert pathologists in centroblast detection.

Bibliography

[1] M. Gurcan, L. Boucheron, A. Can, A. Madabhushi, N. Rajpoot, and B. Yener, "Histopathological image analysis: A review," *IEEE Reviews in Biomedical Engineering*, vol. 2, pp. 147 –171, 2009.

[2] P. A. Kenny, G. Y. Lee, C. A. Myers, R. M. Neve, J. R. Semeiks, P. T. Spellman, K. Lorenz, E. H. Lee, M. H. Barcellos-Hoff, O. W. Petersen, J. W. Gray, and M. J. Bissell, "The morphologies of breast cancer cell lines in three-dimensional assays correlate with their profiles of gene expression," *Molecular Oncology*, vol. 1, no. 1, pp. 84 – 96, 2007.

[3] M. C. Alley, D. A. Scudiero, A. Monks, M. L. Hursey, M. J. Czerwinski, D. L. Fine, B. J. Abbott, J. G. Mayo, R. H. Shoemaker, and M. R. Boyd, "Feasibility of drug screening with panels of human tumor cell lines using a microculture tetrazolium assay," *Cancer Research*, vol. 48, no. 3, pp. 589–601, 1988.

[4] F. Buontempo, T. Ersahin, S. Missiroli, S. Senturk, D. Etro, M. Ozturk, S. Capitani, R. Cetin-Atalay, and M. Neri, "Inhibition of AKT signaling in hepatoma cells induces apoptotic cell death independent of AKT activation status," *Investigational New Drugs*, vol. 29, pp. 1303–1313, 2011. 10.1007/s10637-010-9486-3.

[5] M. Miller and N. Kingsbury, "Image denoising using derotated complex wavelet coefficients," *IEEE Transactions on Image Processing*, vol. 17, pp. 1500 –1511, sept. 2008.

[6] G. Chen, T. Bui, and A. Krzyzak, "Palmprint classification using dual-tree complex wavelets," in *Proceedings of IEEE International Conference on Image Processing*, pp. 2645–2648, Oct 2006.

[7] T. Celik and T. Tjahjadi, "Multiscale texture classification using dual-tree complex wavelet transform," *Pattern Recognition Letters*, vol. 30, no. 3, pp. 331 – 339, 2009.

[8] M. Thamarai and R. Shanmugalakshmi, "Video coding technique using swarm intelligence in 3-d dual tree complex wavelet transform," in *Machine Learning and Computing (ICMLC), 2010 Second International Conference on*, pp. 174 –178, Feb 2010.

[9] P. Loo and N. Kingsbury, "Digital watermarking using complex wavelets," in *Proceedings of IEEE International Conference on Image Processing*, vol. 3, pp. 29 –32, 2000.

[10] I. Selesnick, R. Baraniuk, and N. Kingsbury, "The dual-tree complex wavelet transform," *IEEE Signal Processing Magazine*, vol. 22, pp. 123–151, Nov. 2005.

[11] O. Tuzel, F. Porikli, and P. Meer, "Region covariance: A fast descriptor for detection and classification," in *Computer Vision ECCV 2006* (A. Leonardis, H. Bischof, and A. Pinz, eds.), vol. 3952 of *Lecture Notes in Computer Science*, pp. 589–600, Springer Berlin / Heidelberg, 2006.

[12] D. Tan and S. J. Horning, "Follicular lymphoma: Clinical features and treatment," *Hematology/Oncology Clinics of North America*, vol. 22, no. 5, pp. 863 – 882, 2008. Non-Hodgkin's Lymphomas: New Insights and Therapeutic Strategies.

[13] E. S. Jaffe, N. L. Harris, H. Stein, and J. W. Vardiman, *Pathology and Genetics: Tumours of Haematopoietic and Lymphoid Tissues*. Lyon, France: IARC Press, 2001.

[14] G. E. Metter, B. N. Nathwani, J. S. Burke, C. D. Winberg, R. B. Mann, M. Barcos, C. R. Kjeldsberg, C. C. Whitcomb, D. O. Dixon, and T. P.

Miller, "Morphological subclassification of follicular lymphoma: variability of diagnoses among hematopathologists, a collaborative study between the repository center and pathology panel for lymphoma clinical studies.," *Journal of Clinical Oncology*, vol. 3, no. 1, pp. 25–38, 1985.

[15] O. Sertel, J. Kong, U. Catalyurek, G. Lozanski, J. Saltz, and M. Gurcan, "Histopathological image analysis using model-based intermediate representations and color texture: Follicular lymphoma grading," *Journal of Signal Processing Systems*, vol. 55, pp. 169–183, 2009.

[16] O. Sertel, G. Lozanski, A. Shana'ah, and M. Gurcan, "Computer-aided detection of centroblasts for follicular lymphoma grading using adaptive likelihood-based cell segmentation," *IEEE Transactions on Biomedical Engineering*, vol. 57, pp. 2613 –2616, oct. 2010.

[17] H. Kong, M. Gurcan, and K. Belkacem-Boussaid, "Partitioning histopathological images: An integrated framework for supervised color-texture segmentation and cell splitting," *IEEE Transactions on Medical Imaging*, vol. 30, pp. 1661 –1677, sept. 2011.

[18] T. Lindeberg, "Feature detection with automatic scale selection," *International Journal of Computer Vision*, vol. 30, pp. 79–116, 1998.

[19] D. G. Lowe, "Distinctive image features from scale-invariant keypoints," *International Journal of Computer Vision*, vol. 60, pp. 91–110, 2004.

[20] S. Azari, N. Ahmadi, M. J. Tehrani, and F. Shokri, "Profiling and authentication of human cell lines using short tandem repeat (str) loci: Report from the National Cell Bank of Iran," *Biologicals*, vol. 35, no. 3, pp. 195–202, 2007.

[21] P. Hughes, D. Marshall, Y. Reid, H. Parkes, and C. Gelber, "The costs of using unauthenticated, over-passaged cell lines: how much more data do we need?," *BioTechniques*, vol. 43, pp. 575–586, November 2007.

[22] W. Dirks, R. MacLeod, and H. Drexler, "Ecv304 (endothelial) is really t24 (bladder carcinoma): Cell line cross-contamination at source," *In Vitro Cellular & Developmental Biology - Animal*, vol. 35, pp. 558–559, 1999.

[23] J. Masters, "False cell lines: The problem and a solution," *Cytotechnology*, vol. 39, pp. 69–74, 2002.

[24] R. A. Mackleod, W. G. Dirks, Y. Matsuo, M. Kaufmann, H. Milch, and H. G. Drexler, "Widespread intraspecies cross-contamination of human tumor cell lines arising at source," *International Journal of Cancer*, vol. 83, pp. 555–563, November 1999.

[25] W. G. Dirks and H. G. Drexler, "Authentication of cancer cell lines by dna fingerprinting," *Methods in Molecular Medicine*, vol. 88, no. 2, pp. 43–55, 2004.

[26] J. R. Masters, J. A. Thomson, B. Daly-Burns, Y. A. Reid, W. G. Dirks, P. Packer, L. H. Toji, T. Ohno, H. Tanabe, C. F. Arlett, L. R. Kelland, M. Harrison, A. Virmani, T. H. Ward, K. L. Ayres, and P. G. Debenham, "Short tandem repeat profiling provides an international reference standard for human cell lines," *Proceedings of the National Academy of Sciences*, vol. 98, no. 14, pp. 8012–8017, 2001.

[27] C.-C. Chang and C.-J. Lin, "LIBSVM: A library for support vector machines," *ACM Transactions on Intelligent Systems and Technology*, vol. 2, pp. 27:1–27:27, 2011. Software available at `http://www.csie.ntu.edu.tw/~cjlin/libsvm`.

[28] M. Vilela, J. J. Morgan, and P. A. Lindahl, "Mathematical model of a cell size checkpoint," *PLoS Computational Biology*, vol. 6, p. e1001036, 12 2010.

[29] R. Steuer, S. Waldherr, V. Sourjik, and M. Kollmann, "Robust signal processing in living cells," *PLoS Computational Biology*, vol. 7, p. e1002218, 11 2011.

[30] A. Suhre, T. Ersahin, R. Cetin-Atalay, and A. E. Cetin, "Microscopic image classification using sparsity in a transform domain and bayesian learning," in *19th European Signal Processing Conference*, pp. 1005–1009, 2011.

[31] I. Daubechies, "Orthonormal bases of compactly supported wavelets," *Communications on Pure and Applied Mathematics*, vol. 41, 1988.

[32] S. Mallat, "A theory for multiresolution signal decomposition: the wavelet representation," *IEEE Transactions on Pattern Analysis and Machine Intelligence*, vol. 11, pp. 674–693, Jul 1989.

[33] A. Grossman and J. Morlet, "Decomposition of hardy functions into square integrable wavelets of constant shape," *SIAM J. Math.*, vol. 15, pp. 723–736, 1984.

[34] W. Sweldens, "The lifting scheme: A new philosophy in biorthogonal wavelet constructions," in *Wavelet Applications in Signal and Image Processing III*, pp. 68–79, 1995.

[35] M. Antonini, M. Barlaud, P. Mathieu, and I. Daubechies, "Image coding using wavelet transform," *IEEE Transactions on Image Processing*, vol. 1, pp. 205–220, Apr 1992.

[36] Y.-Q. Zhang and S. Zafar, "Motion-compensated wavelet transform coding for color video compression," *IEEE Transactions on Circuits and Systems for Video Technology*, vol. 2, pp. 285–296, Sep 1992.

[37] D. Sinha and A. Tewfik, "Low bit rate transparent audio compression using adapted wavelets," *IEEE Transactions on Signal Processing*, vol. 41, pp. 3463–3479, dec 1993.

[38] R. Favero, "Compound wavelets: wavelets for speech recognition," in *Time-Frequency and Time-Scale Analysis, 1994., Proceedings of the IEEE-SP International Symposium on*, pp. 600–603, oct 1994.

[39] M. Unser, "Texture classification and segmentation using wavelet frames," *IEEE Transactions on Image Processing*, vol. 4, pp. 1549 –1560, Nov 1995.

[40] M. Do and M. Vetterli, "Wavelet-based texture retrieval using generalized gaussian density and kullback-leibler distance," *IEEE Transactions on Image Processing*, vol. 11, pp. 146 –158, Feb 2002.

[41] D. Donoho and I. Johnstone, "Threshold selection for wavelet shrinkage of noisy data," in *Engineering in Medicine and Biology Society, Engineering Advances: New Opportunities for Biomedical Engineers. Proceedings of the*

16th Annual International Conference of the IEEE, vol. 1, pp. A24–A25, Nov 1994.

[42] C. Demonceaux and D. Kachi-Akkouche, "Motion detection using wavelet analysis and hierarchical markov models," in *Spatial Coherence for Visual Motion Analysis* (W. MacLean, ed.), vol. 3667 of *Lecture Notes in Computer Science*, pp. 64–75, Springer Berlin / Heidelberg, 2006.

[43] B. U. Toreyin, Y. Dedeoglu, U. Gudukbay, and A. E. Cetin, "Computer vision based method for real-time fire and flame detection," *Pattern Recognition Letters*, vol. 27, no. 1, pp. 49–58, 2006.

[44] N. Kingsbury, "The dual-tree complex wavelet transform: A new technique for shift invariance and directional filters," in *Proceedings of IEEE Digital Signal Processing Workshop*, pp. 319–322, 1998.

[45] I. Selesnick, "Hilbert transform pairs of wavelet bases," *Signal Processing Letters, IEEE*, vol. 8, pp. 170–173, June 2001.

[46] R. Kwitt, A. Uhl, M. Hafner, A. Gangl, F. Wrba, and A. Vecsei, "Predicting the histology of colorectal lesions in a probabilistic framework," in *Proceedings of IEEE Computer Society Conference on Computer Vision and Pattern Recognition Workshops (CVPRW)*, pp. 103 –110, June 2010.

[47] R. Kwitt and A. Uhl, "Modeling the marginal distributions of complex wavelet coefficient magnitudes for the classification of zoom-endoscopy images," in *IEEE 11th International Conference on Computer Vision*, pp. 1–8, Oct 2007.

[48] D. Aydogan, M. Hannula, T. Arola, J. Hyttinen, and P. Dastidar, "Texture based classification and segmentation of tissues using dt-cwt feature extraction methods," in *Proceedings of 21st IEEE International Symposium on Computer-Based Medical Systems*, pp. 614 –619, June 2008.

[49] T. Ojala, M. Pietikainen, and T. Maenpaa, "Multiresolution gray-scale and rotation invariant texture classification with local binary patterns," *IEEE Transactions on Pattern Analysis and Machine Intelligence*, vol. 24, pp. 971–987, Jul 2002.

[50] O. Tuzel, F. Porikli, and P. Meer, "Region covariance: A fast descriptor for detection and classification," in *Proc. 9th European Conf. on Computer Vision*, pp. 589–600, 2006.

[51] H. Tuna, I. Onaran, and A. Cetin, "Image description using a multiplier-less operator," *IEEE Signal Processing Letters*, vol. 16, pp. 751–753, Sept 2009.

[52] O. Tuzel, F. Porikli, and P. Meer, "Pedestrian detection via classification on riemannian manifolds," *IEEE Transactions on Pattern Analysis and Machine Intelligence*, vol. 30, pp. 1713–1727, 2008.

[53] Y. Habiboglu, O. Gunay, and A. Cetin, "Flame detection method in video using covariance descriptors," in *Proceedings of IEEE International Conference on Acoustics, Speech and Signal Processing (ICASSP)*, pp. 1817 –1820, May 2011.

[54] C. Ye, J. Liu, C. Chen, M. Song, and J. Bu, "Speech emotion classification on a riemannian manifold," in *Advances in Multimedia Information Processing - PCM* (Y.-M. Huang, C. Xu, K.-S. Cheng, J.-F. Yang, M. Swamy, S. Li, and J.-W. Ding, eds.), vol. 5353 of *Lecture Notes in Computer Science*, pp. 61–69, Springer Berlin / Heidelberg, 2008.

[55] N. Kilic, O. Kursun, and O. Ucan, "Classification of the colonic polyps in ct-colonography using region covariance as descriptor features of suspicious regions," *Journal of Medical Systems*, vol. 34, pp. 101–105, 2010.

[56] N. Otsu, "A threshold selection method from gray-level histograms," *IEEE Transactions on Systems, Man and Cybernetics*, vol. 9, pp. 62 –66, jan. 1979.

[57] R. O. Duda, P. E. Hart, and D. G. Stork, *Pattern Classification*. New York: Wiley-Interscience, 2001.

[58] R. Maree, P. Geurts, J. Piater, and L. Wehenkel, "Random subwindows for robust image classification," in *Proceedings of IEEE Computer Society Conference on Computer Vision and Pattern Recognition*, vol. 1, pp. 34–40, June 2005.

[59] N. Kingsbury, "A dual-tree complex wavelet transform with improved orthogonality and symmetry properties," in *Proceedings of IEEE International Conference on Image Processing*, vol. 2, pp. 375–378, Sept 2000.

[60] N. Kingsbury, "Image processing with complex wavelets," *Phil. Trans. Royal Society London A*, vol. 357, pp. 2543–2560, 1997.

[61] O. Yorulmaz, T. C. Pearson, and A. Çetin, "Detection of fungal damaged popcorn using image property covariance features," *Comput. Electron. Agric.*, vol. 84, pp. 47–52, June 2012.

[62] Y. Shinohara, T. Masuko, and M. Akamine, "Covariance clustering on riemannian manifolds for acoustic model compression," in *Proceedings of IEEE International Conference on Acoustics Speech and Signal Processing (ICASSP)*, pp. 4326–4329, March 2010.

[63] Y. H. Habiboglu, O. Gunay, and A. E. Cetin, "Real-time wildfire detection using correlation descriptors," in *19th European Signal Processing Conference (EUSIPCO 2011), Special Session on Signal Processing for Disaster Management and Prevention*, 2011.

[64] B. E. Boser, I. M. Guyon, and V. N. Vapnik, "A training algorithm for optimal margin classifiers," in *Proceedings of the 5th Annual ACM Workshop on Computational Learning Theory*, pp. 144–152, ACM Press, 1992.

[65] M. Dundar, S. Badve, V. Raykar, R. Jain, O. Sertel, and M. Gurcan, "A multiple instance learning approach toward optimal classification of pathology slides," in *Proceedings of 20th International Conference on Pattern Recognition (ICPR)*, pp. 2732–2735, August 2010.

[66] F. Keskin, T. Ersahin, R. Çetin Atalay, and A. E. Çetin, "Microscopic image classification via CWT-based covariance descriptors using Kullback-Leibler distance," in *Proceedings of IEEE International Symposium on Circuits and Systems (ISCAS)*, May 20-23 2012.

[67] F. Keskin, A. Suhre, T. Ersahin, R. Çetin Atalay, and A. E. Çetin, "Carcinoma cell line discrimination in microscopic images using unbalanced

wavelets," in *Proceedings of 46th Annual Conference on Information Sciences and Systems (CISS)*, 21-23 March 2012.

[68] F. Keskin, A. Suhre, K. Kose, T. Ersahin, R. Çetin Atalay, and A. E. Çetin, "Image classification of human carcinoma cells using complex wavelet-based covariance descriptors," *PLoS ONE*, 2012. submitted.

[69] A. M. Glas, L. Knoops, L. Delahaye, M. J. Kersten, R. E. Kibbelaar, L. A. Wessels, R. van Laar, J. H. J. van Krieken, J. W. Baars, J. Raemaekers, P. M. Kluin, L. J. vant Veer, and D. de Jong, "Gene-expression and immunohistochemical study of specific t-cell subsets and accessory cell types in the transformation and prognosis of follicular lymphoma," *Journal of Clinical Oncology*, vol. 25, no. 4, pp. 390–398, 2007.

[70] K. Belkacem-Boussaid, M. Pennell, G. Lozanski, A. Shana'ah, and M. Gurcan, "Computer-aided classification of centroblast cells in follicular lymphoma," *Analytical and Quantitative Cytology and Histology*, vol. 32 (5), pp. 254–260, October 2010.

[71] O. Sertel, U. Catalyurek, G. Lozanski, A. Shanaah, and M. Gurcan, "An image analysis approach for detecting malignant cells in digitized h&e-stained histology images of follicular lymphoma," in *Proceedings of 20th International Conference on Pattern Recognition (ICPR)*, pp. 273–276, August 2010.

[72] O. Sertel, J. Kong, G. Lozanski, U. Catalyurek, J. H. Saltz, and M. N. Gurcan, "Computerized microscopic image analysis of follicular lymphoma," in *Society of Photo-Optical Instrumentation Engineers (SPIE) Conference Series*, vol. 6915, Apr. 2008.

[73] T. Lindeberg, "On the axiomatic foundations of linear scale-space: Combining semi-group structure with causality vs. scale invariance," 1997. Technical Report.

[74] D. Lowe, "Object recognition from local scale-invariant features," in *Proceedings of the Seventh IEEE International Conference on Computer Vision*, vol. 2, pp. 1150–1157, 1999.

[75] Y. Al-Kofahi, W. Lassoued, W. Lee, and B. Roysam, "Improved automatic detection and segmentation of cell nuclei in histopathology images," *IEEE Transactions on Biomedical Engineering*, vol. 57, pp. 841 –852, April 2010.

[76] J. Byun, M. R. Verardo, B. Sumengen, G. P. Lewis, B. S. Manjunath, and S. K. Fisher, "Automated tool for the detection of cell nuclei in digital microscopic images: Application to retinal images," *Molecular Vision*, vol. 12, pp. 949–960, 2006.

[77] J. Byun, N. Vu, B. Sumengen, and B. Manjunath, "Quantitative analysis of immunofluorescent retinal images," in *Proceedings of 3rd IEEE International Symposium on Biomedical Imaging: Nano to Macro*, pp. 1268–1271, April 2006.

[78] H. Cinar Akakin, H. Kong, C. Elkins, J. Hemminger, B. Miller, J. Ming, E. Plocharczyk, R. Roth, M. Weinberg, R. Ziegler, G. Lozanski, and M. N. Gurcan, "Automated detection of cells from immunohistochemically-stained tissues: application to ki-67 nuclei staining," in *Proceedings of Society of Photo-Optical Instrumentation Engineers (SPIE) Conference Series*, vol. 8315, Feb. 2012.

[79] T. Lindeberg, "Scale-space theory: a basic tool for analyzing structures at different scales," *Journal of Applied Statistics*, vol. 21, no. 1-2, pp. 225–270, 1994.

[80] J. Koenderink, "The structure of images," *Biological Cybernetics*, vol. 50, pp. 363–370, 1984.

[81] J. Babaud, A. P. Witkin, M. Baudin, and R. O. Duda, "Uniqueness of the gaussian kernel for scale-space filtering," *IEEE Transactions on Pattern Analysis and Machine Intelligence*, vol. PAMI-8, pp. 26–33, Jan. 1986.

[82] T. Lindeberg, "Detecting salient blob-like image structures and their scales with a scale-space primal sketch: A method for focus-of-attention," *International Journal of Computer Vision*, vol. 11, pp. 283–318, 1993.

[83] M. Gurcan, Y. Yardimci, A. Cetin, and R. Ansari, "Detection of microcalcifications in mammograms using higher order statistics," *IEEE Signal Processing Letters*, vol. 4, pp. 213 –216, Aug. 1997.

[84] T. Akgul, M. Sun, R. Sclahassi, and A. Cetin, "Characterization of sleep spindles using higher order statistics and spectra," *IEEE Transactions on Biomedical Engineering*, vol. 47, pp. 997–1009, Aug. 2000.

[85] R. M. Haralick, K. Shanmugam, and I. Dinstein, "Textural features for image classification," *IEEE Transactions on Systems, Man and Cybernetics*, vol. SMC-3, pp. 610–621, nov. 1973.

[86] M. M. Galloway, "Texture analysis using gray level run lengths," *Computer Graphics and Image Processing*, vol. 4, no. 2, pp. 172–179, 1975.

[87] A. Vedaldi and B. Fulkerson, "Vlfeat – an open and portable library of computer vision algorithms," in *Proceedings of the 18th Annual ACM International Conference on Multimedia*, 2010.